Dropwise Condensation of Water and Low Surface Tension Fluids on Structured Surfaces

by

Yajing Zhao

B. E., Energy and Power Engineering (2016)
Xi'an Jiaotong University, China

Submitted to the Department of Mechanical Engineering in
Partial Fulfillment of the Requirements for the
Degree of Master of Science in Mechanical Engineering
at the
Massachusetts Institute of Technology
June 2018

Signature of Author: ………………………………………………………………….……

Department of Mechanical Engineering
May 25, 2018

Certified by: ………………………………………………………………………..……

Evelyn N. Wang
Gail E. Kendall Professor of Mechanical Engineering
Thesis Supervisor

Accepted by: …………………………………………………………………….……

Rohan Abeyaratne
Chairman, Department Committee on Graduate Theses

Dropwise Condensation of Water and Low Surface Tension Fluids on Structured Surfaces

by

Yajing Zhao

Submitted to the Department of Mechanical Engineering on May 25th, 2018,
in Partial Fulfillment of the Requirements for the Degree of Master of Science

Abstract

Condensation is a ubiquitous process often observed in nature and our daily lives. The large amount of latent heat released during the condensation process has been harnessed in many industrial processes such as power generation, building heating and cooling, desalination, dew harvesting, thermal management, and refrigeration. Condensation has two modes: dropwise mode and filmwise mode. Although it has been known for decades that dropwise condensation outperforms filmwise condensation in heat transfer owing to the droplet shedding effects which can efficiently reduce thermal resistance, filmwise condensation still dominates industrial applications currently due to the high costs, low robustness and technical challenges of manufacturing dropwise coatings. During water condensation, dropwise mode can be readily promoted with thin hydrophobic coatings. Superhydrophobic surfaces made out of hydrophobic coatings on micro- or nano-engineered surfaces have shown further heat transfer enhancement in dropwise condensation of water; however, the applications of these micro- or nanoscale structured surface designs have been restricted by the high manufacturing expenses and short range of subcooling limit. Recent studies have shown that the combination of millimeter sized geometric features and plain hydrophobic coatings can effectively manipulate droplet distribution of water condensate, which provides opportunities to locally facilitate dropwise condensation at relatively low manufacturing expenses as compared to those delicate micro- and nano-structured hydrophobic surfaces. Low surface tension fluids such as hydrocarbons pose a unique challenge to achieving dropwise condensation, because common hydrophobic coatings are not capable of repelling low surface tension fluids. Recent development in lubricant infused surfaces (LIS) offers promising solutions to achieving dropwise condensation of low surface tension fluids by replacing the solid-condensate interface in conventional hydrophobic coatings with a smooth lubricant-condensate

interface. However, only a few experimental studies have applied LIS to promoting dropwise condensation of low surface tension fluids (γ as low as 15 mN/m).

In this work, we investigated dropwise condensation of both water ($\gamma \approx 72$ mN/m) and a low surface tension fluid, namely butane ($\gamma \approx 13$ mN/m) on structured surfaces. For water condensation, we studied the effects of millimeter sized geometric structures on dropwise condensation heat transfer under two different environments: pure vapor and an air-vapor mixture. Our experimental results show that, although convex structures enable faster droplet growth in an air-vapor mixture, the same structures impose the opposite effect during pure vapor condensation, hindering droplet growth. We developed a numerical model for each case to predict the heat flux distribution along the structured surface, and the model shows good agreement with experimental results. This work demonstrates that the effects of geometric features on dropwise condensation are not invariable but rather dependent on the scenario of resistances to heat and mass transfer in the system. For butane condensation, based on a design guideline we recently developed for lubricant infused surfaces, we successfully designed an energy-favorable combination of lubricant and structured solid substrate, which was further demonstrated to promote dropwise condensation of butane.

The fundamental understanding of dropwise condensation of water and low surface tension fluids on structured surfaces developed in this study provides useful guidelines for condensation applications including power generation, desalination, dew harvesting, and thermal management.

Thesis Supervisor: Evelyn N. Wang
Title: Associate Department Head for Operations and Gail E. Kendall Professor, Mechanical Engineering

Acknowledgements

I would like to express my deepest gratitude and appreciation to my advisor, Professor Evelyn N. Wang. I thank her for offering me the invaluable opportunity to join the lovely family of Device Research Laboratory. My life at MIT has been an incredibly delightful journey with the company of my amazingly supportive labmates. We share many joyful memories about not only working in the lab but also having fun in various group activities. None of this would have been possible without Evelyn's great leadership. In the past two years, I have seen myself becoming more resilient and fearless when confronting frustrating setbacks in both research and life. Knowing that I would probably have given up several attempts in the face of those obstacles with deep regrets if Evelyn had not encouraged me to keep holding on, I am deeply thankful for her continuous guidance, support and patience. I also have benefited a lot from Evelyn's brilliant perspective in dealing with people. She is a very nice person who always appreciates different personalities and never compares her students. Instead, she cares about us in different ways. I feel fortunate to have her as my advisor.

I have been extremely privileged to have Dr. Daniel J. Preston as my mentor since I joined the Device Research Laboratory. I had little experimental skills before I came here. Dan took me under his wing and taught me every single technique that I lacked with tremendous patience. Dan always inspires me to work hard by setting himself as a role model. As an international student coming from the other side of this planet, I grew up with a completely different culture and language as compared to Dan. I was the kind of person who would only fully open her heart to very few friends and would never initiate a conversation with strangers at social events. However, Dan found a way to open up my inner world and brought out the outgoing nature in me. He is one of the very first friends I have made at MIT, and many other friends of mine were also introduced to me by him. He encouraged me to engage in conversations, and showed me the social etiquette at conferences and other social occasions. I was immature and somewhat thoughtless before, probably because I was an only child. Nevertheless, my daily interactions with Dan have unconsciously developed so many interpersonal skills in me that generally make me a better human being. To me, Dan is like my elder brother, regardless of our different races, colors, or national origins. I could not wish for a better mentor than Dan. As of the writing of this thesis, he had just been granted a professorship at Rice University, and the honor could not have been more deserved.

I'm also greatly thankful for other lab members in the Device Research Laboratory. I would like to express my special thanks to Lin and Yangying, who first introduced me to the lab and made the following magic journey become possible. Kyle and Dion have also provided me with generous guidance for my research on condensation, and I feel grateful for having the opportunity to learn so much from them. Colin, Youngsup

and Lenan have been reliable friends of mine since we joined the lab together in 2016. I appreciate their constant support along the way and look forward to growing together with them over the next few years. Of course, someone who has explored flammables with me and worked alongside me against several deadlines – Sam, thanks for your solid support. I never imagined all of the happiness I would be surrounded with before I joined this lab, and I feel so blessed to be a part of this family. Thank you, DRL!

Although they are not directly related to this work, I would love to give my sincere thanks to my mentors before I came to MIT. Professor Ronald K. Hanson at Stanford University was the first to recognize my academic potential, raising me up to more than I could be. I am forever indebted to him for his unreserved guidance, care and encouragement. Professor Jiangfeng Wang at Xi'an Jiaotong University was my direct advisor in my undergrad years. I thank him for giving me the precious opportunity to work on his team and helping me publish my first first-author paper back in 2016.

I also very much appreciate my dear friends outside the lab who have made my time here at MIT colorful and complete. Foremost, someone who has always been there with me through thick and thin, both my roommate and my "semi"-labmate, Qian – thank you. Yunjo, Clara, Jae, Andrew, Yuwei, Omar, Qing, Jiawei, David, Laureen, Ruoran, and Yu, who have given me tremendous help and support during the qual study period – thank you so much for having my back during the cold and stressful days. Shahd was the first one who showed me the friendliness and splendidness of MIT during the Open House week and has helped me in many ways since I came here; I feel happy and honored to have her as my friend. I have been highly fortunate to get to know many amazing people from RK lab, MIT MEGA Women, and GAME Tennis Leagues; I appreciate every fulfilling moment they have brought to my life: Yvana, Andrea, Rebecca, and Danielle, just to name a few. Last but not least, a girl who shares the same birthday with me, pursuing a PhD in Chemistry at Harvard – Shucong – has become a treasured friend since we met. I thank her for her care, support, and the eye-opening knowledge I have learned with her in Professor Joanna Aizenberg's APPHY235 class.

Finally, I owe a great deal to my family. In retrospect, I was unconditionally supported by my parents to make every decision following my heart. I would not change a thing about how I was raised. Everything good about me came from my extraordinary mom and dad. Words cannot express my deep gratitude and love towards them. This work is dedicated to my parents.

Table of Contents

List of Figures

List of Tables

Chapter 1

1. Introduction

1.1 MOTIVATION

Condensation is a useful approach for energy transport due to the large amount of latent heat released during the phase change process. Condensation of water vapor has been routinely observed in nature [1-3] and commonly utilized in a wide range of applications such as desalination systems [4, 5], steam cycles [6, 7], water harvesting [8, 9] and nuclear reactors [1-3, 10, 11]. Condensation of low surface tension fluids such as refrigerants and hydrocarbons also plays an important role in refrigeration cycles [12, 13] and natural gas processing [14, 15]. In these applications, enhancement of the condensation heat and mass transfer performance can significantly contribute to energy efficiency, economic performance, and environmental sustainability of the overall system. Filmwise condensation (Figure 1) is standard in industrial applications due to the high surface energy of common condenser materials, but this mode of condensation suffers from its intrinsic barrier to heat transfer created by the condensed liquid film. On the other hand, dropwise condensation, which has been demonstrated to exhibit up to an order of magnitude higher heat transfer coefficients (Figure 2) compared to filmwise condensation [16], has attracted much research interest since its discovery in 1930 [17].
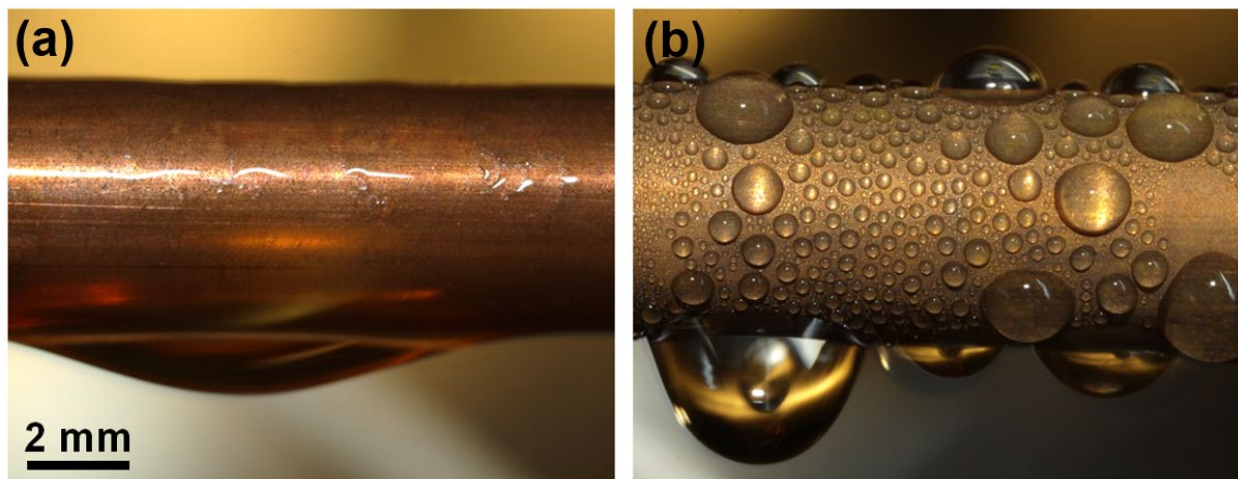
Figure 1. Filmwise condensation on a bare copper condenser tube (a) and dropwise condensation on a copper tube functionalized with a monolayer hydrophobic coating (b), adapted from [18].
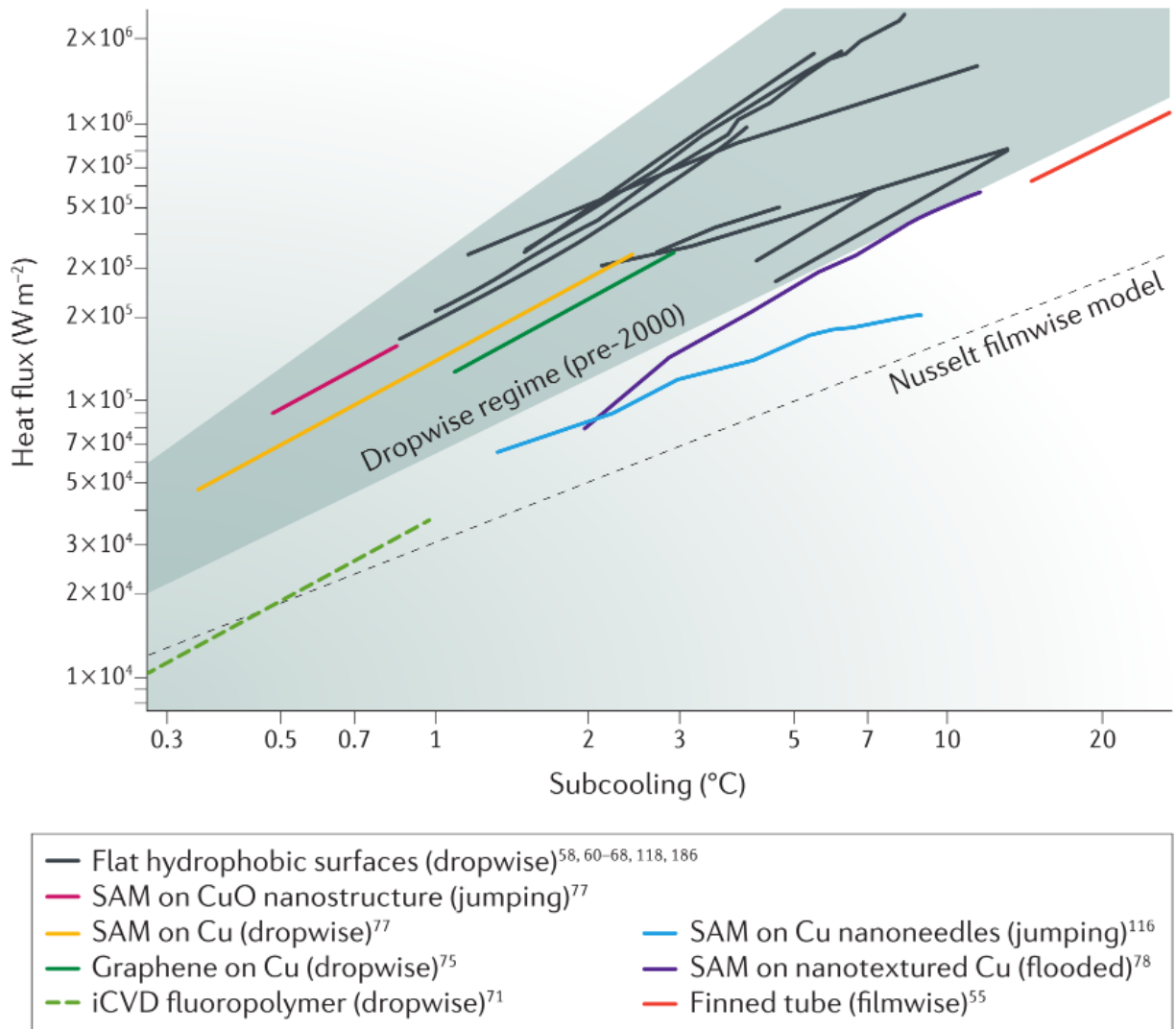
Figure 2. Water condensation heat flux as a function of subcooling for a fixed vapor temperature of 100°C, adapted from [3]. Dropwise condensation experiments conducted on flat hydrophobic surfaces before 2000 are plotted in dark grey lines grouped within a shaded 'dropwise regime' region ; other condensation experiments with surface modification via roughing and coatings are plotted in color; and the Nusselt filmwise condensation model is plotted as a dashed grey line for comparison.

1.2   BACKGROUND

The performance enhancement obtained by dropwise condensation is due to the gravity-induced removal of discrete droplets upon growing to a critical size near the capillary length, allowing renucleation and growth of small droplets; therefore, facilitating droplet growth plays a critical role in dropwise condensation. As such, droplet growth has been studied at great length, both theoretically and experimentally. An early dropwise condensation theory combined the heat transfer rate through a single drop with the expression for drop size distribution to obtain the condensation heat flux on the surface [19].

Following this work, more advanced models have been developed by considering precise descriptions for droplet size distribution [20] and the effect of large contact angles [21, 22]. Among experimental studies, a variety of micro- and nanoscale surface structures have been used to manipulate droplet growth. High droplet mobility and rapid droplet removal have been demonstrated on nanowires [23], nanocones [24], and hierarchical structures [25]. In addition, spatial control of micro-droplet arrays has been achieved on micro-pillar arrays [26], mesh-screen structures [27] and hybrid surfaces [28]. Furthermore, superhydrophobic nanotextured copper oxide surfaces [29-31] have been developed to enable micrometer-sized droplets to jump off of a surface regardless of gravity, which yields a higher condensation heat transfer coefficient compared with state-of-the-art dropwise condensing surfaces [18, 32-35].

1.2.1   DROPWISE CONDENSATION OF WATER ON MILLIMETRIC GEOMETRIC FEATURES

In contrast to micro- or nano- scale structures that require relatively intricate and costly manufacturing processes and are often prone to physical wear and destruction, recent studies have reported that millimeter-sized convex structures can effectively manipulate dropwise condensation of water. Park et al. [36] designed slippery asymmetric bumps (Figure 3) which significantly facilitate droplet growth and departure and thereby show a sixfold-higher droplet growth rate compared to flat surfaces. Keeping track of droplet size distribution on the bumpy surface, they experimentally demonstrated that millimetric bumps alone can enhance condensation on the top of the bumps. Medici et al. [37] also studied the effect of millimeter-sized geometric features (corners, edges, grooves and scratches) on droplet growth during condensation (Figure 4). They concluded that millimetric surface discontinuities can modify droplet growth rates such that droplets near outer corners and edges grow faster than those near inner corners, in agreement with Park's result. They also mentioned that this geometric effect disappears when condensing on a substrate with poor thermal conductivity. However, they attributed this phenomenon to the low thermal conductivity of the substrate material and did not consider the effects of the material property on the overall thermal resistance network, which is the critical aspect to the condensation profile.
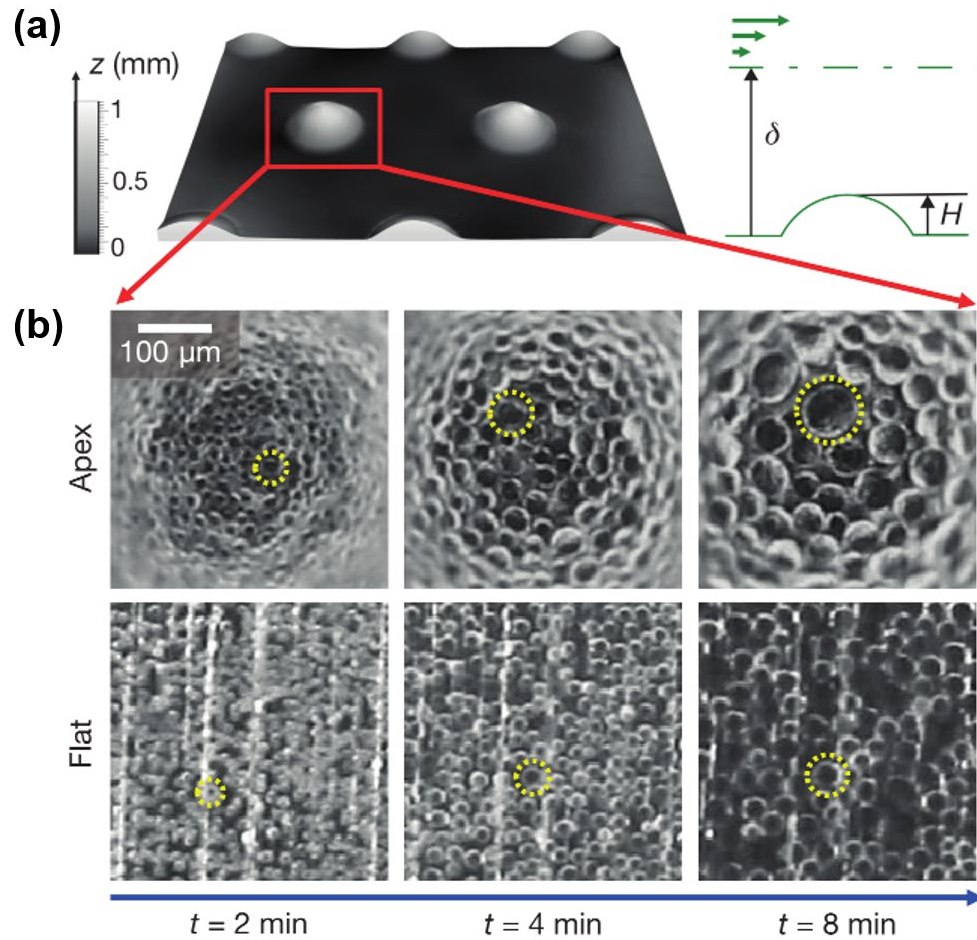
Figure 3. Dropwise condensation of water on millimetric convex bumps vs. flat surfaces, adapted from [36]. (a) A profilometer image of a hexagonal array of millimetric spherical-cap-shaped bumps (left), and the boundary of the diffusion layer (green dash-dotted line, right), within which diffusion is the dominant mechanism of mass transport (depletion layer thickness $\delta \gg H$). (b) Time-lapsed images of droplets growing on the apex of the bumps (top row) compared to a flat region with the same height H (bottom row).
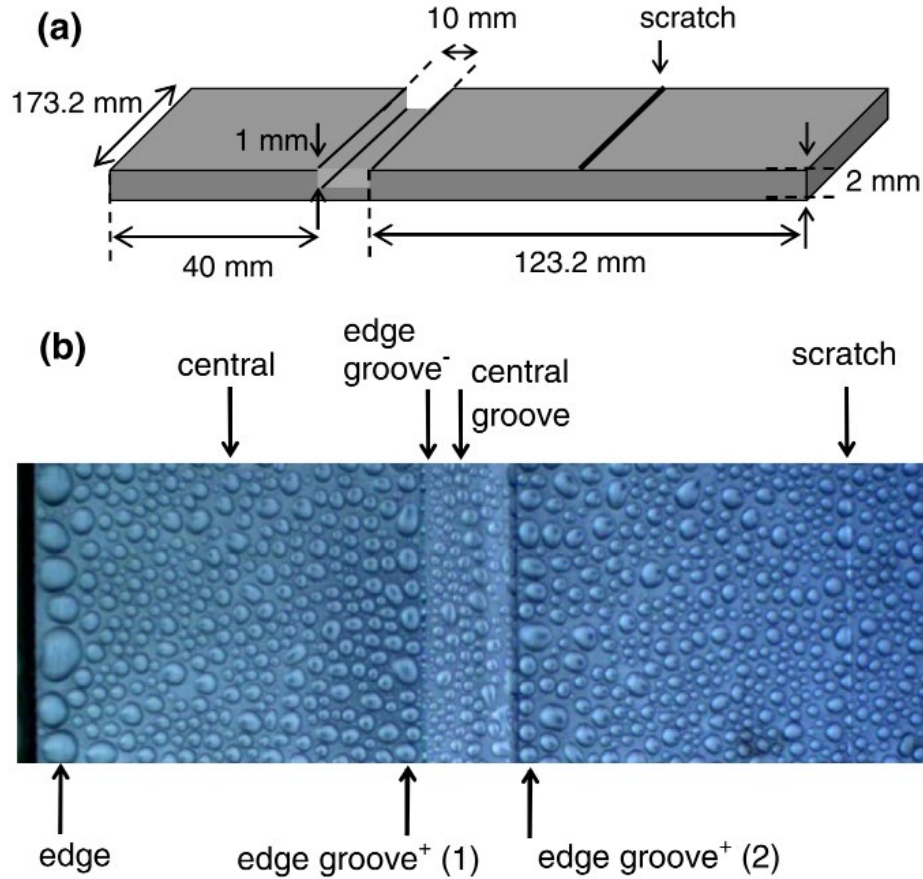
Figure 4. Dropwise condensation of water on millimetric grooves, corners and edges, adapted from [37]. (a) Schematic of the structured condenser substrate. (b) Droplet distribution on the structured condenser surface during the condensation process.

Indeed, these two studies of millimeter-scale geometric effects on dropwise condensation are of great importance, since the condensation situation that is being considered there, i.e., vapor condensation in air, is ubiquitous in a variety of applications such as desalination [38], water harvesting [9], air cooling [39] and waste heat recovery [40]. However, these previous works did not take into account that the condensation performance is affected not only by geometric features but also by vapor conditions, i.e., the presence of non-condensable gases (air, in this case). Vapor condensation in the presence of non-condensable gases (NCGs) is hindered by the required vapor diffusion across a boundary layer introduced by NCGs accumulation near the liquid-vapor interface [41-43]. It has been demonstrated that NCGs introduce additional heat and mass transfer resistance and therefore significantly degrade condensation performance in both the filmwise and dropwise modes [44]. In an early experimental demonstration of the filmwise mode [45], a decrease of nearly 50% in condensation heat transfer coefficient was observed in the presence of 0.5% NCG volume fraction. In accordance with this, a numerical study on laminar filmwise condensation

[46] showed that the presence of a few percent of NCGs can substantially reduce condensation heat transfer and furthermore introduce a dramatic change in the temperature profile. The temperature of the liquid-vapor interface was calculated to be as high as the bulk vapor temperature in the absence of NCGs, but decreased to almost the cold wall temperature in the presence of 2% mass fraction of NCGs. A similar temperature profile altered by NCGs was observed in an experimental study where filmwise condensation with and without NCGs inside a vertical tube was investigated [47], and the authors attributed the altered temperature profile to the prominent influence of NCGs on the thermal resistance network. The wall temperature was observed to be close to the bulk vapor temperature in the pure-steam condensation mode because the gas side had negligible thermal resistance; however, it approached the coolant temperature when the NCGs on the gas side almost fully controlled the overall thermal resistance network. This viewpoint of NCGs-influenced thermal resistance network was also explored in an experimental study [48] where the dropwise and the filmwise modes resulted in a similar range of heat transfer rates when condensing air-steam mixtures, owing to the governing role of the air-rich diffusion boundary layer in the thermal resistance network dominating that of the condensation modes.

Prior work has compared condensation heat transfer performance with and without NCGs [45-47, 49], and recent work has shed light on geometrically enhanced dropwise condensation with NCGs [36, 37], but geometric effects on dropwise condensation performance with and without NCGs have not been considered simultaneously.

1.2.2 DROPWISE CONDENSATION OF LOW SURFACE TENSION FLUIDS ON LUBRICANT INFUSED SURFACES (LIS)

Although dropwise condensation of water vapor could be readily promoted via various surface designs, the properties of these surfaces are limited by their inability to induce dropwise condensation in systems where low surface tension fluids such as hydrocarbons and refrigerants are being used. Fluids with low surface tensions are expected to exhibit low contact angles and spread over conventional hydrophobic surfaces, resulting in filmwise condensation, because conventional hydrophobic coatings that used to repel water ($\gamma \approx 72$ mN/m) are hardly capable of repelling fluids with low surface tensions ($\gamma < 30$ mN/m). Previous studies have proposed to use reentrant and doubly-reentrant structured surfaces to repel low surface tension impinging fluids [50, 51]; however, these structured surface designs do not work for condensation of low surface tension fluids where nanoscale nucleation of the condensates could occur within the structures and consequently render the surface hydrophobic [28, 52].

Recently developed idea of utilizing a thin film of lubricating liquids trapped in micro/nanoporous media to repel impinging fluids (Figure 5), i.e., lubricant infused surfaces (LIS), as independently reported by LaFuma and Quére and Wong et al. [53, 54], has paved a novel way to achieve dropwise condensation with low-surface-tension fluids. By taking advantage of the chemical homogeneity and physical smoothness of the liquid-liquid interface of LIS, dropwise condensation with low surface tension fluids such as toluene, octane, hexane and pentane have been experimentally demonstrated and a heat transfer enhancement up to five times over filmwise mode has been measured [55, 56]. In addition to experimental demonstrations on condensation performances of LIS, some other studies have focused on understanding the mechanisms behind the performance, such as investigations on wetting behaviors of droplets [57], droplet growth and distribution [58], and design guidelines for the combination of condensates, lubricants, and solids [59], etc.
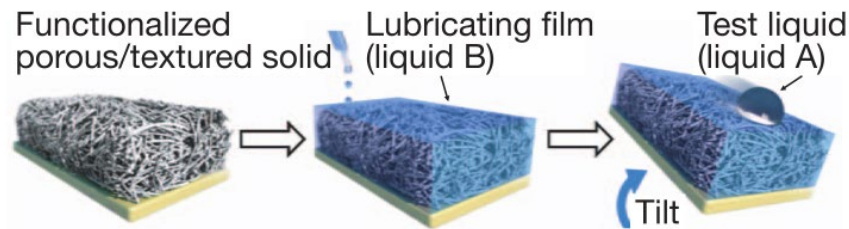
Figure 5. Schematics showing the fabrication of lubricant infused surfaces by infiltrating a porous solid substrate with a low-surface-energy, chemically inert liquid to form a physically smooth and chemically homogeneous lubricating film on the surface of the substrate, adapted from [54].

Butane, one of the most typical natural gas liquid products from a gas processing plant [60], has extremely low surface tension ($\gamma \approx 13$ mN/m) and therefore poses a unique challenge to achieving dropwise condensation. According to the design guideline for LIS developed in a recent study [59], dropwise condensation of butane is promising upon appropriate combination of solid substrate and infused lubricant. In the same study, LIS with repellency to impinging liquid butane was successfully developed, where silicon micro-pillars and hexafluoroisopropanol (6F-IPA) were used as the solid substrate and the lubricant, respectively (Figure 6). However, experimental demonstration of dropwise condensation of butane on LIS has not been reported yet in the literature.
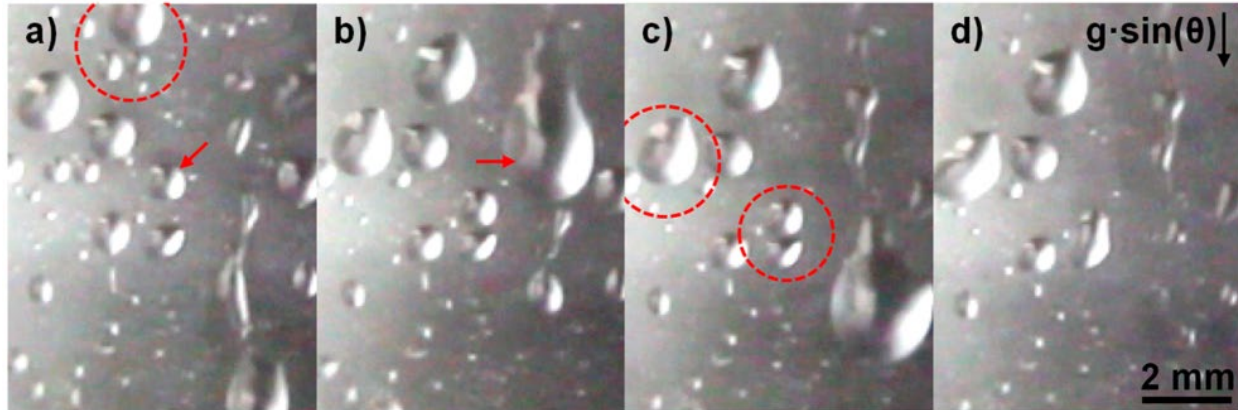
Figure 6. Behavior of liquid butane impinging on a LIS made of 6F-IPA infused silicon micropillars, adapted from [59]. Photos (a) – (d) are time lapse images of droplets moving on the LIS after being sprayed on the surface. The dashed red circles indicate when droplet coalescence events are about to occur, and the red arrows indicate droplets sliding on the surface.

1.3   THESIS OBJECTIVES AND OUTLINE

The objective of this thesis to experimentally investigate dropwise condensation with water and low surface tension fluids on structured surfaces. For water condensation, we investigated the effects of millimetric geometric features on dropwise condensation under different vapor conditions by examining the heat transfer performance in two cases (air-vapor mixture vs. pure vapor). To provide an improved understanding of the physical phenomenon, we developed numerical models for both case studies based on analysis of the thermal resistance network involved in the heat and mass transfer process. The good agreement between experimental results and modeling predictions demonstrates that the enhancement effect of geometric features on dropwise condensation is not absolute, but rather is determined by the specific thermal resistance scenario involved in the given case of heat and mass transfer, which can be completely altered by the presence of NCGs. For dropwise condensation of low surface tension fluids, we designed a lubricant infused surface (LIS) to achieve dropwise condensation of an extremely low surface tension hydrocarbon, namely butane, based on a design guideline recently developed for LIS. Dropwise condensation of butane was successfully demonstrated on the designed LIS. The structure of this thesis is outlined below:

In Chapter 1, the motivation for studying dropwise condensation of water and low surface tension fluids is discussed. Previously studied modes of condensation and significant contributions to the field are explored. Recent advances in facilitating dropwise condensation through structured surfaces are reviewed.

In Chapter 2, dropwise condensation of water on a millimetric structured surface under two different vapor conditions, i.e., pure vapor and air-vapor mixture, are experimentally investigated. Numerical models are also developed to compare with the experimental results.

In Chapter 3, dropwise condensation of an extremely low surface tension fluids, namely butane ($\gamma \approx 13$ mN/m), is experimentally demonstrated using a specifically designed lubricant infused surface.

In Chapter 4, perspectives on the current work are summarized and future directions are discussed.

Chapter 2

2. Dropwise Condensation of Water on Millimetric Geometric Features

2.1 MATERIALS AND METHODS

2.1.1 CONDENSATION SUBSTRATE

A metal block 2.03 cm in width, 1.83 cm in height, and 2.11 cm in length, including a bump 0.38 cm in width, 0.38 cm in height, and 2.11 cm in length on the top surface, was milled to serve as the geometric-featured substrate for the present study (Figure 7). In order to guarantee that heat would conduct from the top to the bottom surface of the block during condensation and to prevent condensation on the sidewalls, thermal insulation for the block sidewalls was provided with a 0.5 mm-thick polyetherimide (Ultem) frame snugly fit around the sides of the condensation block.

In order to demonstrate opposite condensation scenarios on the same substrate under the two vapor conditions (air-vapor mixture vs. pure vapor), we deliberately designed reverse thermal resistance scenarios under the two conditions by selecting titanium as the block material upon a preliminary thermal resistance analysis. The thermal resistance of the titanium block can be estimated using a simplified 1D conduction model by the following equation:

$$R_{th} = \delta / k ,$$
(1)

where δ denotes the characteristic thickness of the geometric feature in the conduction direction (0.38 cm), and k is the thermal conductivity of the block material (for titanium, k =15.6 W/(mK)). Consequently, the thermal resistance of the condensation block is on the order of $10^{-4}\,m^2K/W$, almost 2 orders of magnitude between the characteristic thermal resistances of condensation in pure vapor and condensation in an air-vapor mixture, which can be estimated by the following equation:

$$R_{th} = 1 / h ,$$
(2)

where h is the condensation heat transfer coefficient ($1/h$ is on the order of 10^{-6}~10^{-5} m^{2}K/W for pure vapor and 10^{-2}~10^{-1} m^{2}K/W for the air-vapor mixture) [6, 16, 38, 40, 61].
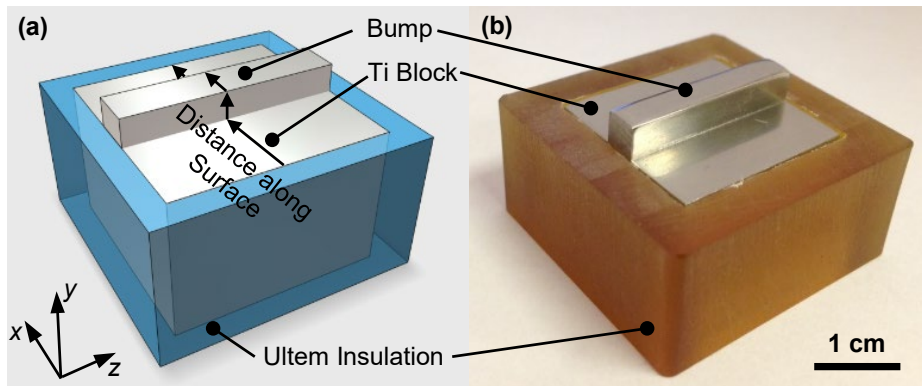
Figure 7. A titanium block including a rectangular bump on the top surface was milled to serve as the condenser surface. The block was thermally insulated by polyetherimide. The schematic and a photo of the condenser surface with surrounding insulation are shown in a) and b), respectively, adapted from [62].

In order to achieve dropwise condensation, the titanium block was functionalized by depositing a fluorinated silane (trichloro(1H, 1H, 2H, 2H-perfluorooctyl)-silane, Sigma-Aldrich) in the vapor phase. Detailed procedures of the coating deposition can be found in the Appendix.

We performed wetting characterization of the sample with a goniometer to capture images while injecting water from a droplet on the flat surface of the sample, then analyzing the images with ImageJ software to determine the advancing contact angle. A typical contact angle measurement result given by ImageJ analysis of an image captured in the goniometer is shown in Figure 8.
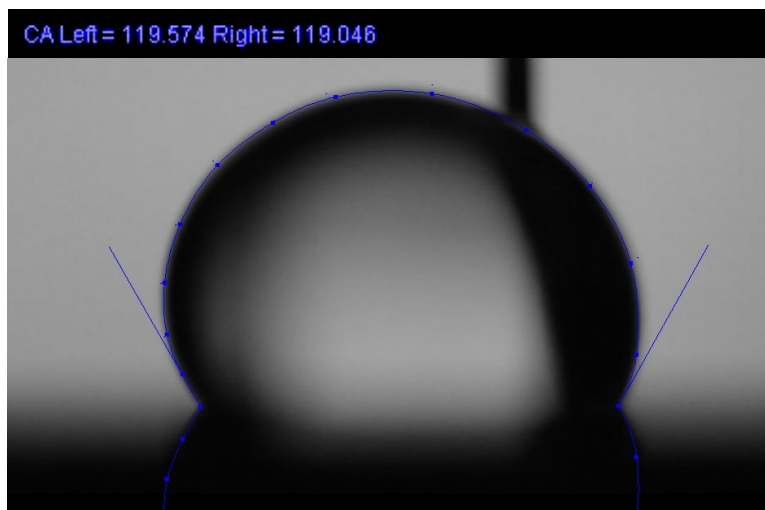
Figure 8 Advancing contact angle measurement from an image captured in the goniometer and processed by ImageJ software.

21

The advancing contact angle was measured to be 120.2±3.1 degrees, which is in a good agreement with previous publications [18, 24, 63]:

Table 1. Advancing contact angle of water on trichloro(1H, 1H, 2H, 2H-perfluorooctyl)-silane coating in previous literature

Reference	θ_a
J.D. Smith, A.J. Meuler, H.L. Bralower, R. Venkatesan, S. Subramanian, R.E. Cohen, G.H. McKinley, K.K. Varanasi, Hydrate-phobic surfaces: fundamental studies in clathrate hydrate adhesion reduction, Physical chemistry chemical physics : PCCP, 14(17) (2012) 6013-6020.	$120.8 \pm 0.8°$
N. Miljkovic, R. Enright, Y. Nam, K. Lopez, N. Dou, J. Sack, E.N. Wang, Jumping-droplet-enhanced condensation on scalable superhydrophobic nanostructured surfaces, Nano Lett, 13(1) (2013) 179-187.	$123.4 \pm 2.5°$
T. Mouterde, G. Lehoucq, S. Xavier, A. Checco, C.T. Black, A. Rahman, T. Midavaine, C. Clanet, D. Quere, Antifogging abilities of model nanotextures, Nat Mater, (2017).	$120 \pm 2°$

2.1.2   EXPERIMENTAL SETUP

We tested the heat transfer performance of the condensation block under two vapor conditions (air-vapor mixture vs. pure vapor) in a controlled condensation chamber (Figures 9) in which the total pressure can be accurately measured.

The custom environmental chamber used for this work (Kurt J. Lesker) consists of a stainless steel frame with a door (sealed with a rubber gasket), two viewing windows, and apertures for various components. Resistive heater lines were wrapped around the exterior of the chamber walls to prevent condensation at the inside walls and then insulated on the exterior walls. The output power of the resistive heater lines was controlled by a voltage regulator (Variac). Two thermally insulated stainless steel water flow lines (Swagelok) were fed into the chamber *via* a KF flange port (Kurt J. Lesker) to supply cooling water to the chamber from a large capacity chiller (System III, Neslab). A flowmeter (7 LPM MAX, Hedland) with an accuracy of $\pm$ 2% was integrated along the water inflow line.

A secondary stainless steel tube line was fed into the chamber *via* a KF adapter port that served as the flow line for the incoming water vapor supplied from a heated steel water reservoir. The vapor reservoir was wrapped with a rope heater (120 W, Omega) and thermally insulated to limit heat losses to the environment. The access tubes were welded to the vapor reservoir, each with independently-controlled valves. The first valve (Diaphragm Type, Swagelok), connecting the bottom of the reservoir to the ambient, was used to fill

the reservoir with water. The second valve (BK-60, Swagelok), connecting the top of the reservoir to the inside of the chamber, provided a path for vapor inflow. K-type thermocouples were located along the length of the water vapor reservoir to monitor temperature.

A bellows valve (Kurt J. Lesker) was attached to the chamber to serve as a leak port between the ambient and inside of the chamber. In order to monitor temperatures within the chamber, J-type thermocouple bundles were connected through the chamber apertures *via* a thermocouple feed through (Kurt J. Lesker). A pressure transducer (925 Micro Pirani, MKS) was attached to monitor pressure within the chamber. The thermocouple bundles and the pressure transducer were both electrically connected to an analog input source (9205&9213, National Instruments), which was interfaced to a computer for data recording. A second bellows valve (Kurt J. Lesker) was integrated onto the chamber for the vacuum pump, which brought down the chamber to vacuum conditions prior to vapor filling. A liquid nitrogen cold trap was incorporated along the line from the chamber to the vacuum which served to remove any moisture from the pump-down process and ultimately assist in yielding higher quality vacuum conditions. A tertiary bellows valve (Kurt J. Lesker) was integrated on a T fitting between the vacuum pump and liquid nitrogen reservoir to connect the vacuum line to the ambient to release the vacuum line to ambient conditions once pump down was achieved. In order to visually capture data, a digital SLR camera (EOS Rebel T3, Canon) was placed in line with the 5" viewing windows on the chamber. The schematic of the exterior of the chamber setup is depicted in Figure 9 (a). Images of the front and rear of the chamber setup are shown in Figures 9 (b) and (c), respectively.
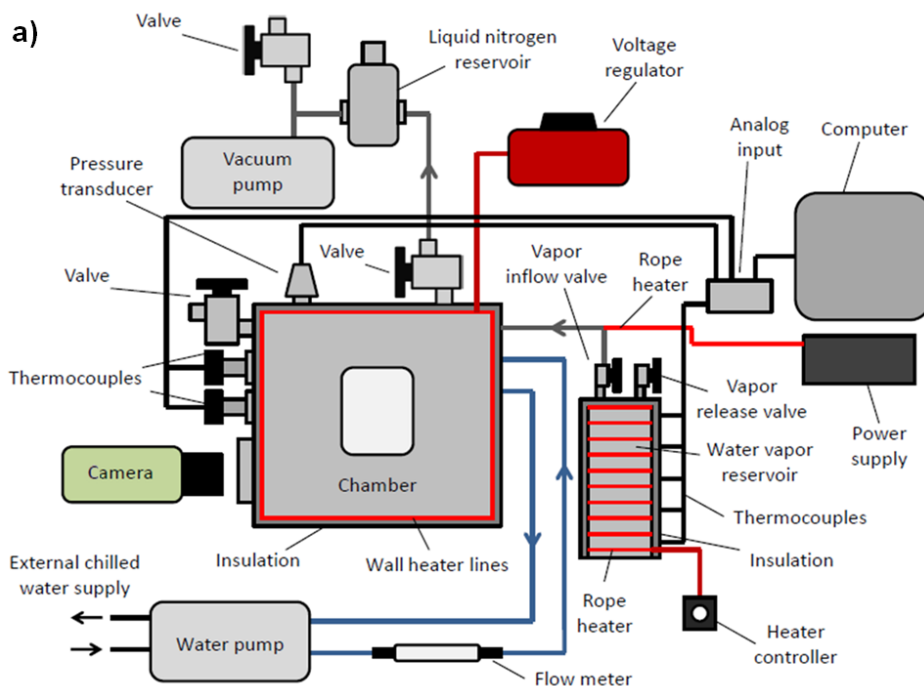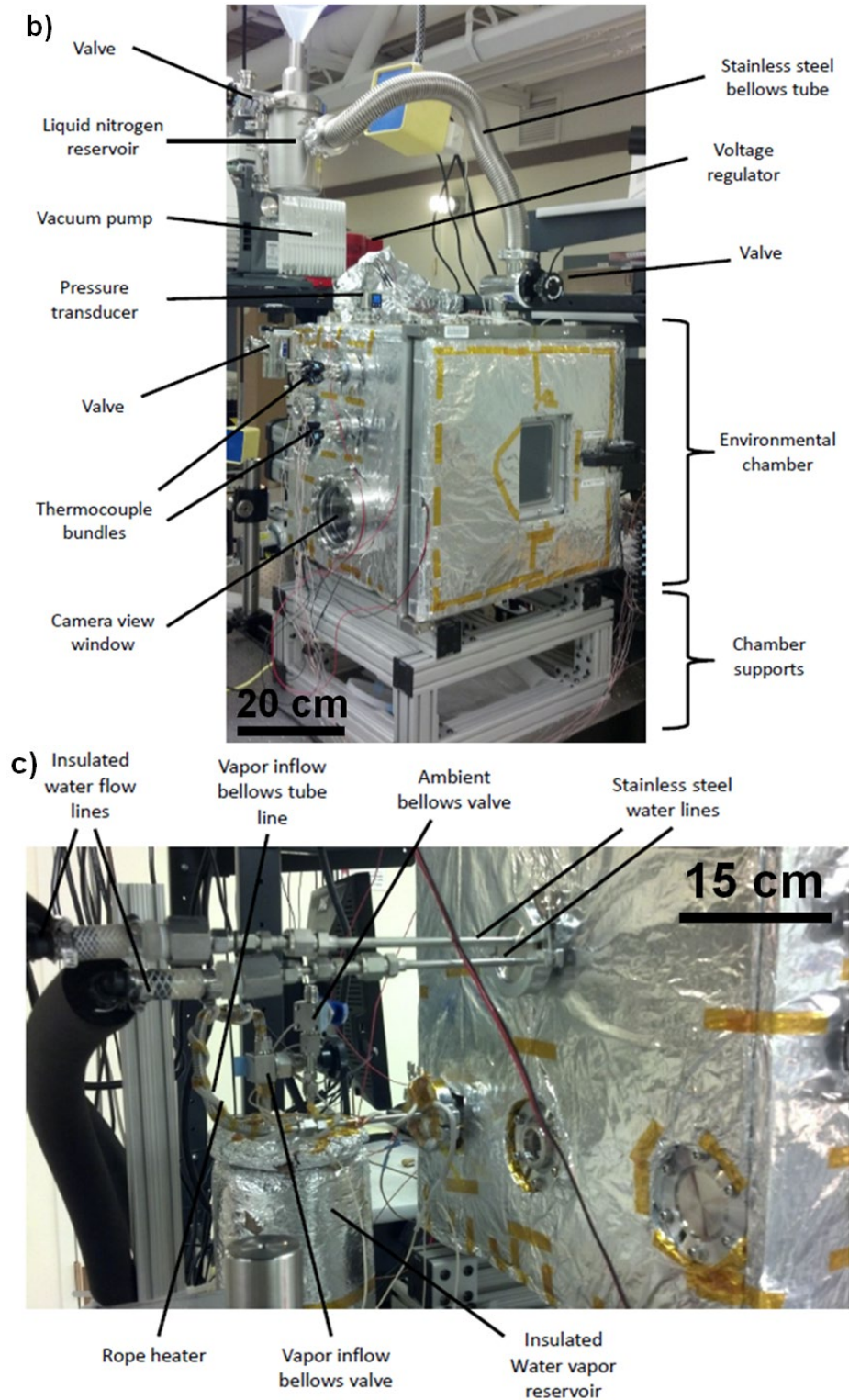
Figure 9. Chamber setup for water condensation experiments, adapted from [18]. (a) Schematic of experimental setup (not to scale). (b) Image of the experimental setup shown from the front (camera and data acquisition system not shown). (c) Image of the experimental setup from the rear of the chamber showing the cooling water inlet and outlet and water vapor reservoir.

24

The schematic (not to scale) and the images taken from the outside and the inside of the condensation chamber for the condensation test rig are shown in Figure 10 a), b), and c), respectively. Pure vapor was supplied from a heated water reservoir to the chamber. Vapor condensation took place on the top surface of the horizontally placed condensation block, where droplets grew without removal of condensate due to the absence of favorable gravity. The titanium condensation block was cooled down by being attached to a 2.54 cm×2.54 cm×1.27 cm copper block cooling stage through a thin layer of double sided copper tape. Just beneath the copper tape, a small groove was carved on the cooling stage surface from its center to the midpoint of one of its edges, in which a J-type thermocouple was tightly embedded to monitor the local temperature. Considering the small thickness (0.09 mm) and the high conductivity ($\geq$5 W/(mK)) of the copper type, the thermal resistance of the copper tape, which could be estimated as $R_{\text{th,copper tape}} = \delta_{\text{copper tape}} / k_{\text{copper tape}} \leq 1.8 \times 10^{-6}$ m^{2}K/W, is much less than the thermal resistance of the titanium block (on the order of 10^{-4} m^{2}K/W). Therefore, the temperature drop through the copper tape could be neglected and it is justifiable to regard the measurement from the center thermocouple as the bottom surface temperature of the titanium block, T_b. A 6.35 mm-diameter hole was drilled through the cooling stage, into which a copper cooling tube with the same outside diameter was inserted for internal chiller water flow. Visualization of the condensation development was achieved through a viewing window on the chamber, where the camera was placed in line with the viewing window. A mirror tilted at an angle of 45° was fixed above the condensation block to reflect an image of the top surface of the block for the camera to capture both the sidewall and the top surface of the bump. For the air-vapor mixture condensation experiment, both dry bulb temperature and wet bulb temperature of the bulk air-vapor mixture were measured by J-type thermocouples suspended in the chamber. The relative humidity calculated by the measured dry bulb and wet bulb temperatures were further compared with the reference value measured by a humidity meter (RH820, OMEGA) placed in the chamber.
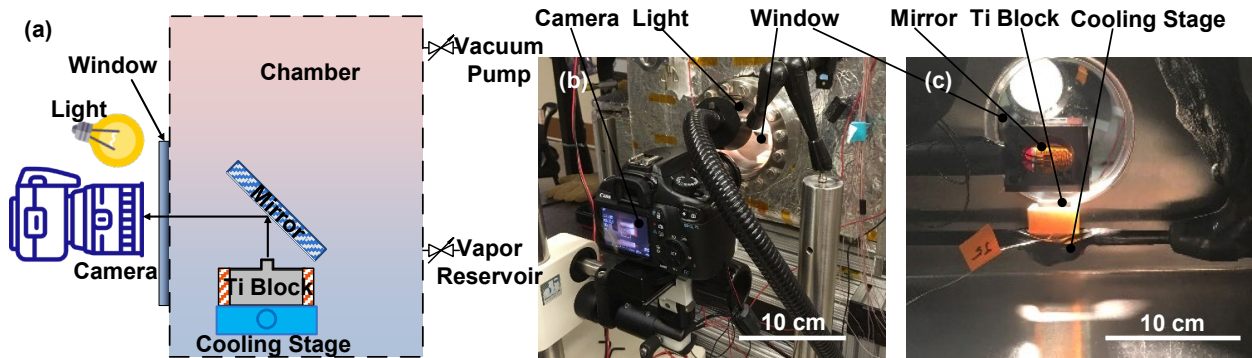
Figure 10. The schematic (not to scale) and the images taken from the outside and the inside of the chamber for the condensation test rig are shown in (a), (b) and (c), respectively, adapted from [62].

2.1.3 EXPERIMENTAL PROCEDURES

A set of strict procedures was followed throughout the experiments. For both case studies (air-vapor mixture and pure vapor), the same preparatory steps including preheating the chamber, degassing the water vapor reservoir and installing the test sample were followed.

The first step was to turn on the voltage regulator to heat the condensation chamber walls up to a temperature over 35°C such that vapor would not condense on the chamber wall. Meanwhile, the water vapor reservoir was degassed through the following procedures. Initially, 3.5 liters of DI water (99% full) was filled into the reservoir using a syringe through a vapor release valve on the reservoir. Then, the vapor release valve was closed and a vapor inflow valve connecting the water vapor reservoir to the chamber was opened, when the rope heater around the reservoir was turned on with its maximum power (120 W). Two K type thermocouples were installed in the water vapor reservoir monitoring the temperature at the top and at the bottom section of the reservoir respectively. The top section temperature was measured to be higher than the bottom section temperature, because of the water thermal-mass present at the middle/bottom section. Thus, we ensured that the regions in the reservoir with higher thermal capacity were brought to a sufficiently high temperature for boiling. Once boiling occurred and both the top section temperature and the bottom section temperature of the reservoir were measured to be higher than 95°C for more than 10 minutes, the vapor inflow valve was closed. The excess water that spilled inside the chamber during the degassing process was removed. In order to install the test sample onto the rig, the two ends of the copper cooling tube were connected to two 90-degree male elbow connecters on the rig. After all adapters/connecters were tightened without leaks that could influence vapor conditions, the bellow tubes were connected to the water lines for circulating cooling water and the test setup was placed onto the steel supports. Then, the mirror was fixed onto the steel supports facing towards the test sample with a tilting angle of 45° to reflect the top surface of the bumpy structure to the camera placed in line with the viewing window outside the chamber. All of the tubes for cooling water flow inside the chamber except the section inside the cooling stage were insulated and the mirror was attached to a heating pad (power 5W, 3M), in order to avoid vapor condensation on them.

Both the experiments (air-vapor mixture condensation and pure vapor condensation) were carried out in the condensation chamber with the chamber door closed. The difference between these two experiments is the control over the vapor condition (i.e., the content of NCGs). In the air-vapor mixture case, the bellows valve connecting the inside of the chamber to the outside ambient was kept open in order to maintain an ambient pressure inside the chamber with inlet air. In the pure vapor case, the bellows valve was kept closed throughout the experiment, and the condensation chamber was evacuated to a vacuum of $P<1.0$ Pa to

eliminate NCGs prior to introducing the pure vapor from the reservoir. This vacuum condition was reached by following a standard pump-down procedure. First, the liquid nitrogen cold trap was filled to about half capacity. The ambient exposed valve connecting the chamber and the vacuum pump was closed and the valve connected to the liquid nitrogen cold trap was opened. Then, the vacuum pump was turned on, starting the pump-down process, during which the chamber pressure was continuously monitored. Typically, the satisfactory vacuum conditions (0.5 Pa<P<1 Pa) was reached after one hour of the pump-down process.

After the vapor condition was satisfied in each case (air-vapor mixture vs. pure vapor), the heater around the water vapor reservoir was turned down to 5% power and the vapor inflow valve was slowly opened until the operating conditions were achieved. Simultaneously, the camera was turned on to record condensation development. A light source (KL 2500 LCD, SCHOTT) was properly fixed next to the camera outside the viewing window of the chamber for supplementary illumination. It took about two minutes of full operation to achieve steady state performance. For the air-vapor mixture case, the steady state condition was obtained at a bulk fluid temperature of 56°C with a relative humidity of 80%. For the pure vapor condensation experiment, a steady state at vapor pressure of 6 kPa was maintained, which is a typical operation pressure for power plant condensers [12, 64].

2.1.4   NUMERICAL MODELING

In order to understand the experimental results, we modeled each of the environmental conditions explored in the present work. Numerical models for dropwise condensation in both the air-vapor mixture and in pure vapor were developed for comparison with experimental results based on the following assumptions:

(1) Condensation occurred at a steady state.
(2) Variations in temperature or vapor concentration in the z direction (Figure 7) were negligible (2D model).
(3) Adiabatic conditions (no heat transfer or mass transfer in the horizontal direction) were applied to the two vertical boundaries of the considered 2D region, which is justifiable for the symmetric situation where an array of the same geometric features is used.
(4) In the case of air-vapor mixture condensation, the gas region occupied the largest thermal resistance and therefore the condensation block could be treated as isothermal at the bottom surface temperature T_b. Mass transfer of water vapor occurred in a diffusion boundary layer where convection effects were negligible [65].

(5) In the case of pure vapor condensation, the gas region had negligible thermal resistance compared with the solid region. Therefore, the vapor was assumed to be saturated homogeneously in the chamber (including at the liquid-vapor interface on the block) at the bulk temperature T_∞.

Note that here we approximated the surface temperature of the block T_s to be equivalent to the bottom surface temperature of the block T_b in the air-vapor mixture case and to the saturation temperature of the bulk vapor T_∞ in the pure vapor case, based on analysis of the thermal resistances. During the experiments, we used this approximation instead of measuring the surface temperature directly because adding thermocouples onto the block surface would affect the droplet growth rate measurement during the image processing work.

For the air-vapor mixture condensation, large amounts of NCGs accumulated near the condensation surface, forming a boundary layer within which mass diffusion of water vapor was driven by the concentration gradient of water vapor. For the present study, the boundary layer thickness was approximated using the method of shape factor, based on the analogy between the heat conduction problem and the mass diffusion problem described as follows.

Consider a conduction heat transfer problem where a thin rectangular plate with length L and width W ($W>L$) at a uniform temperature T_1 is attached to a semi-infinite medium with a far-field temperature of T_2, as shown in Figure 11.
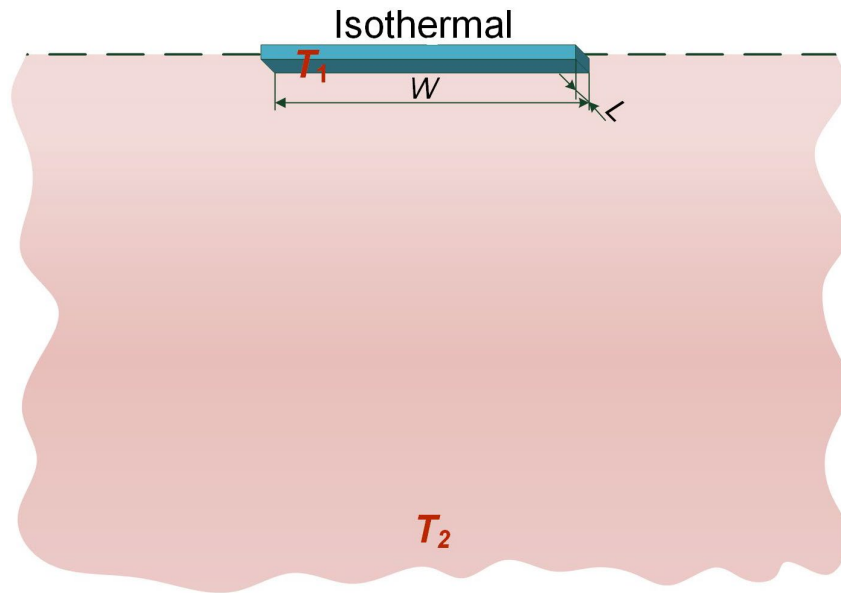
Figure 11. A thin rectangular plate of length L (into page), width W with a uniform temperature of T_1 attached to a semi-infinite medium having isothermal surface. The far-field temperature and the isothermal surface temperature for the semi-infinite medium are the same as T_2.

At steady state and with a constant thermal conductivity of the rectangular plate, the governing equation for this heat transfer problem can be simplified as:

$$\frac{\partial^2 T}{\partial x^2} + \frac{\partial^2 T}{\partial y^2} + \frac{\partial^2 T}{\partial z^2} = 0 \tag{3}$$

In addition, two boundary conditions need to be satisfied:

$$T_{\text{plate}} = T_1; T_{\text{far-field}} = T_2. \tag{4}$$

Thereby, Equation (3) along with boundary conditions (4) completely describe the conduction heat transfer problem mentioned above.

For a steady-state conduction problem where heat is conducted between two isothermal surfaces (or objects), the conduction shape factor S is defined such that

$$\dot{Q} = kS\Delta T, \tag{5}$$

where $\dot{Q}$ denotes the total amount of heat being conducted, k is the thermal conductivity of the material within which heat is transferred, and ΔT represents the temperature difference between the two isothermal surfaces (or objects).

For the case of a thin rectangular plate at T_1 exchanging heat with a semi-infinite medium at T_2, as shown in Figure 12, the conduction shape factor has been given as [66]:

$$S = \frac{\pi W}{\ln(4W/L)}, (W > L). \tag{6}$$

Therefore, the total amount of heat being conducted can be calculated as:

$$\dot{Q} = kS\Delta T = \frac{\pi W k \Delta T}{\ln(4W/L)}. \tag{7}$$

Now consider the mass diffusion problem in the case of air-vapor mixture condensation in the current study. Seeing that the bumpy geometric feature is small compared to the whole condensation block and that the condensation block can be treated as isothermal according to assumption (4), we can simplify the condensation block to a thin, 2.11 cm×2.03 cm plate with a vapor concentration of c_s at its surface, being attached to a semi-infinite medium with a far-field vapor condensation of c_∞.
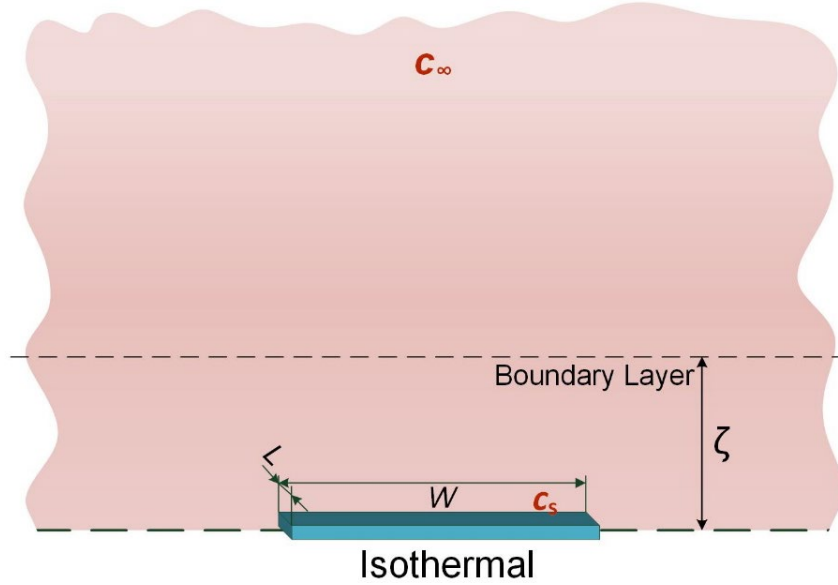
Figure 12. Simplified schematic for vapor condensation on the block in the presence of air. The block is simplified as a 2.11 cm×2.03 cm thin plate with a constant vapor concentration of c_s at its surface. The air-vapor mixture has a far-filed vapor concentration of c_∞. Mass transfer mainly occurs through vapor diffusion in a near-surface boundary layer of thickness.

A schematic for the diffusion problem is shown in Figure 12. At steady state and with a constant diffusion coefficient, the governing equation for this mass transfer problem can be simplified as:

$$\frac{\partial^2 c}{\partial x^2} + \frac{\partial^2 c}{\partial y^2} + \frac{\partial^2 c}{\partial z^2} = 0. \tag{8}$$

In addition, two boundary conditions need to be satisfied:

$$c_{\text{plate}} = c_s; c_{\text{far-field}} = c_\infty. \tag{9}$$

Equation (8) and boundary conditions (9) provide a complete description for the diffusion mass transfer problem.

From a comparison between the governing equations and boundary conditions for the conduction heat transfer problem and the diffusion mass transfer problem mentioned above, it is obvious that these two problems are analogous to each other in mathematics, and hence should have analogous forms of solutions. Therefore, it is reasonable to utilize the shape factor in the conduction problem to approximate the boundary layer thickness in the diffusion problem, as described below.

On the one hand, as an analogy to Equation (7), the total vapor molecules being transferred per unit time through diffusion can be calculated as:

$$\dot{J} = DS\Delta c = \frac{\pi W D \Delta c}{\ln(4W/L)}. \tag{10}$$

On the other hand, under the assumption that mass transfer mainly occurs within a diffusion boundary layer with thickness ζ [36, 65], the total vapor mass being transferred can be derived based on Fick's law:

$$\dot{J} = A\left(D\frac{\Delta c}{\zeta}\right) = (LW)\left(D\frac{\Delta c}{\zeta}\right), \tag{11}$$

where A denotes the surface area of the plate and equals to the product of W and L.

Combining Equations (10) and (11) gives a diffusion boundary layer thickness of 0.92 cm. In the numerical modeling, we approximated the value to be 1 cm as the boundary layer thickness, which is in a good agreement with previous studies [36, 37]. The vapor diffusion within the boundary layer followed:

$$\frac{\partial c}{\partial t} + \vec{\nabla} \cdot \vec{j} = 0, \tag{12}$$

where the first term represents the variation of vapor concentration with time and was set as zero under assumption (1). $\vec{j}$ is the diffusion flux of water vapor, which can be determined by Fick's law:

$$\vec{j} = -D\vec{\nabla}c, \tag{13}$$

where D is the diffusion coefficient of vapor in air, which is related to temperature and pressure. For simplicity, a constant value of 3.0×10^{-5} m^2/s was assigned to D [67], due to the small range of variation in temperature and pressure considered in the present study.

In order to solve the concentration profile of water vapor in the gas region, the following boundary conditions were applied: (i) c at the bottom of the gas region equaled to c_s, corresponding to the saturation

state of water vapor at the top surface temperature of the condensation block T_s, which was approximated to be as same as T_b due to assumption (4); (ii) c beyond the diffusion boundary layer equaled to c_∞, corresponding to the concentration of the bulk air-vapor mixture with temperature, total pressure and relative humidity measured from the experiment; and (iii) adiabatic conditions on the two vertical boundaries.

The complete vapor concentration profile in the gas region was solved through a finite element method (schematically shown in Figure 13) by iterating until convergence. Once the concentration profile was determined, we derived the heat flux distribution along the top surface of the condensation block combining the mass flux distribution with density and latent heat of the water vapor.

For the pure vapor condensation, the water vapor had negligible thermal resistance compared to the titanium condensation block, as discussed in section 2.1.1. Hence, we could assume that the top surface temperature of the block equaled to the saturation temperature of the bulk vapor, and then derived the temperature profile inside the condensation block using the conduction equation:

$$\rho c_p \frac{\partial T}{\partial t} + \vec{\nabla} \cdot \vec{q} = 0, \tag{14}$$

where the first term represents the variation of block temperature with time and was assigned zero under assumption (1). $\vec{q}$ is the heat flux through the condensation block, which was calculated by Fourier's law:

$$\vec{q} = -k\vec{\nabla}T \tag{15}$$

In order to solve the temperature profile in the condensation block, the following boundary conditions were applied: (i) T at the bottom surface of the block equaled to the value measured from the experiment; (ii) T at the top surface of the block T_s equaled to T_∞, corresponding to the saturation temperature of the bulk vapor; and (iii) adiabatic conditions on the two vertical boundaries.

Similar to solving the vapor concentration profile in the gas region, the complete temperature profile of the condensation block was solved through a finite element method (schematically shown in Figure 13) under the constant curvature constraint by iterating until convergence. Heat flux distribution along the top surface of the condensation block was then derived from the block temperature profile.
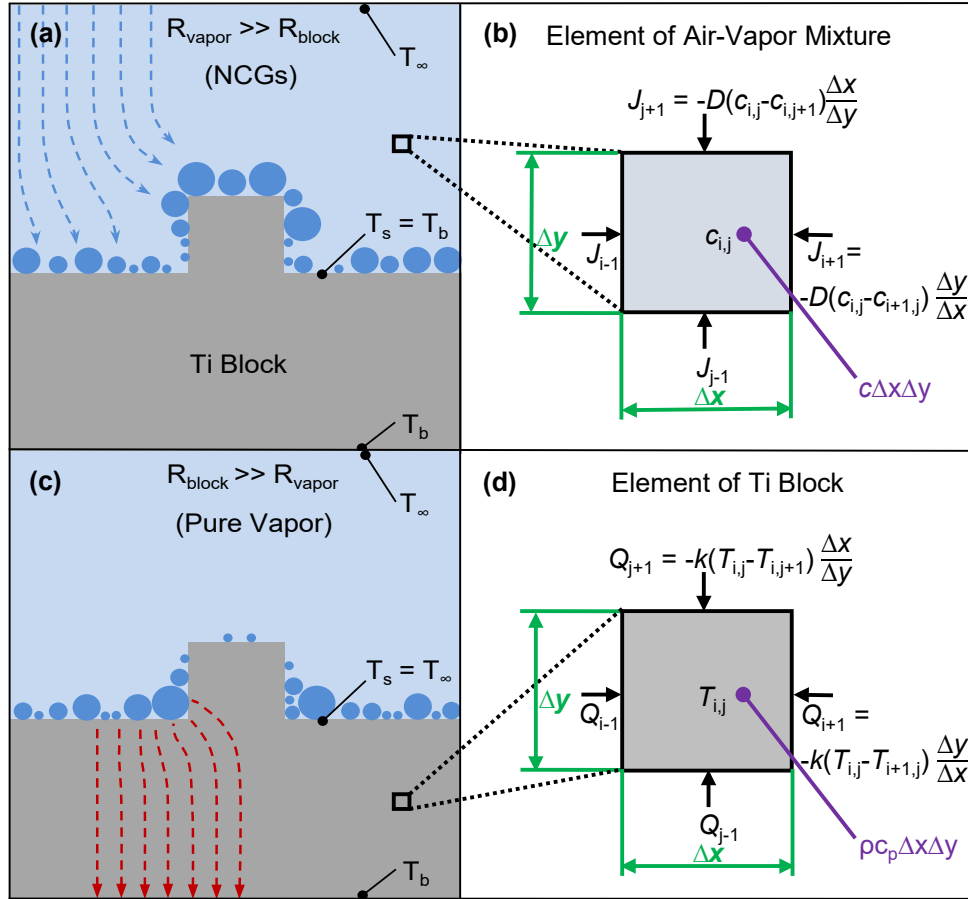
Figure 13. Schematics of the numerical models for dropwise condensation with and without NCGs, adapted from [62]. For the air-vapor mixture case, the gas region dominates the thermal resistance, thus T_s was equal to T_b and the concentration profile was determined by the diffusion equation, as illustrated by the boundary conditions and the governing equations shown in (a) and (b). For the pure vapor case, the solid region dominated the thermal resistance and thus T_s was equal to T_∞ and the concentration profile was determined by the conduction equation, as illustrated by the boundary conditions and the governing equations shown in (c) and (d).

2.2   RESULTS AND DISCUSSION

2.2.1   CONDENSATION PROFILE ON THE MILLIMETRIC STRUCTURED SURFACE

Droplet growth on the top surface of the substrate was visually recorded throughout the condensation experiments. Images of the condensation development on the substrate's top surface with air-vapor mixture and with pure vapor are shown in Figure 14 (a) and (c), respectively. The upper images in the figures show the reflection of the block's top surface in the mirror, and the lower images show the sidewall of the bump. In both cases the substrate displayed dropwise condensation of water vapor, while the condensation rate and the droplet size distribution differed. When exposed to air, water vapor condensed mostly on the top

surface of the bump, especially at the outer edges of the bump, but few condensed droplets were found in the inner corners of the bump, as shown in Figure 14 (a). This observation agrees with those from previous studies about geometric effects on dropwise condensation [36, 37], demonstrating that the bumpy geometric feature provides local enhancement on dropwise condensation. However, in the pure vapor condensation experiment, the droplet size distribution pattern was reversed: vapor was observed to condense mostly in the inner corners of the bump, while little vapor condensed on the top surface of the bump, as shown in Figure 4 c), which demonstrates that the bump has a local degradation effects on dropwise condensation. These results indicate that the same geometric feature with the same material property (in this study, the bump) can impose completely opposite enhancement effects on dropwise condensation under different vapor conditions (air-vapor mixture vs. pure vapor).

The condensation profile in the two case studies as discussed above could be determined by the concentration profile in the gas region (in the air-vapor mixture case) or the temperature profile in the solid region (in the pure vapor case), which was numerically solved based on the analysis of the thermal resistance network. The vapor concentration profile in the diffusion boundary layer for the air-vapor mixture case and the temperature profile in the condensation block for the pure vapor case, solved by the numerical models, are shown in Figure 14 (b) and (d), respectively. For the air-vapor mixture condensation, the largest thermal resistance existed in the gas region due to the presence of a large amount of NCGs. Hence, the bottom boundary of the gas region just above the condensation block was treated as isothermal at T_b and the water vapor concentration there was fixed as a constant corresponding to the saturation condition. The condensation profile could be determined from vapor diffusion driven by the concentration gradient in the gas region. As a result, vapor preferably condensed on the outer edges of the bump where vapor concentration gradient reached the maximum value. In contrast to the case of the air-vapor mixture condensation, in the pure vapor condensation experiment, pure vapor had a negligible thermal resistance compared to the condensation substrate. Thus, the upper boundary of the solid region just below the water vapor was treated as isothermal at T_∞ and the condensation profile could be determined from the heat conduction driven by temperature gradient in the solid region. Consequently, in the pure vapor case, vapor condensation was most likely to occur in the inner corners of the bump where the temperature gradient reached the maximum value.
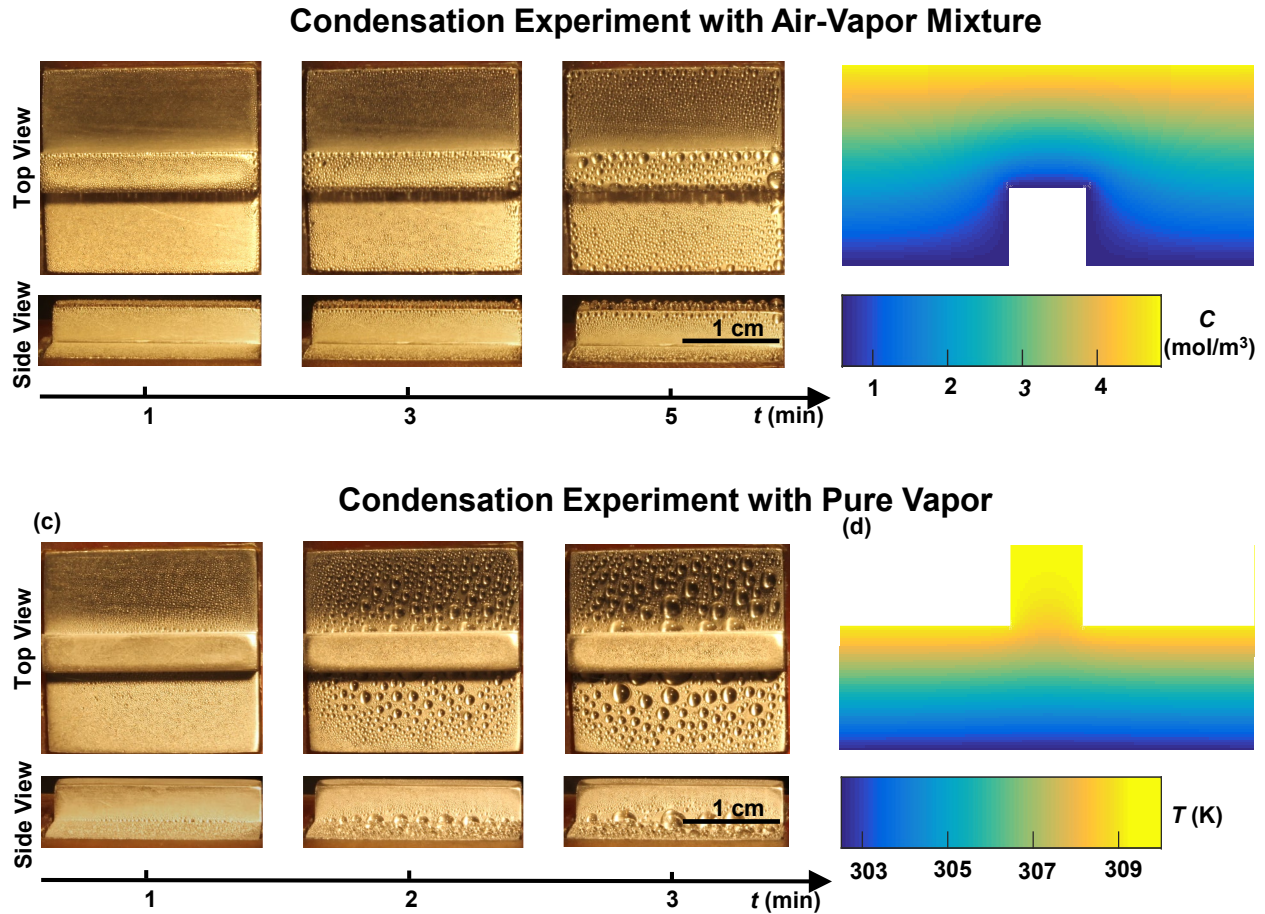
Figure 14. Condensation profile of two case studies (air-vapor mixture vs. pure vapor). (a) Time-lapsed photographs of condensation development on the bumpy condensation substrate in the presence of air. (b) Numerical calculation of concentration profile in the air-vapor diffusion boundary layer for the case of air-vapor mixture condensation. (c) Time-lapse photographs of condensation development on the bumpy condensation substrate with pure vapor. (d) Numerical calculation of temperature profile in the condensation block for the case of pure vapor condensation.

2.2.2 CONDENSATION HEAT TRANSFER PERFORMANCE ON THE MILLIMETRIC STRUCTURED SURFACE

In order to quantify the condensation heat transfer performance in the experiments and to compare it with numerical modeling results, the heat flux distribution along the top surface of the condensation substrate was extracted from experimental data through image processing. Images for droplet growth development were continuously captured every 5 seconds for over 1000 seconds after condensation reached a steady state. The condensate mass increased almost linearly with time for the early stage of dropwise condensation where droplet coalescence did not significantly impact the heat transfer performance [39]. Thus, the condensation rate (mass per unit time) on the condensation substrate was reasonably obtained by dividing the total condensate mass difference between two selected times (within the early stage) by the time interval.

35

In order to distinguish local heat transfer performance, the apparent area on the top surface of the condensation block (in the images) was evenly divided into several grids within which heat flux could be obtained from condensation rate.

For each case of the condensation experiments (i.e., air-vapor mixture or pure vapor), two photographs captured at different time points during the early stage of the steady state dropwise condensation were carefully selected for image processing. In order to evaluate the local heat transfer performance, the apparent top surface of the condensation block in each photograph was evenly divided into 22 rows, as shown in Figure 15. For each row, the center 1/5 part was selected as the representative grid for calculating condensation rate in that row. The reasons for this simplification include: (i) The variations in temperature in the z direction (Figure 7) were assumed to be negligible (2D model), thus ideally each column should have the same condensation rate; (ii) Heat loss to the insulation frame in z direction was inevitable in reality, and the center part experienced the least undesirable heat loss, as expected.
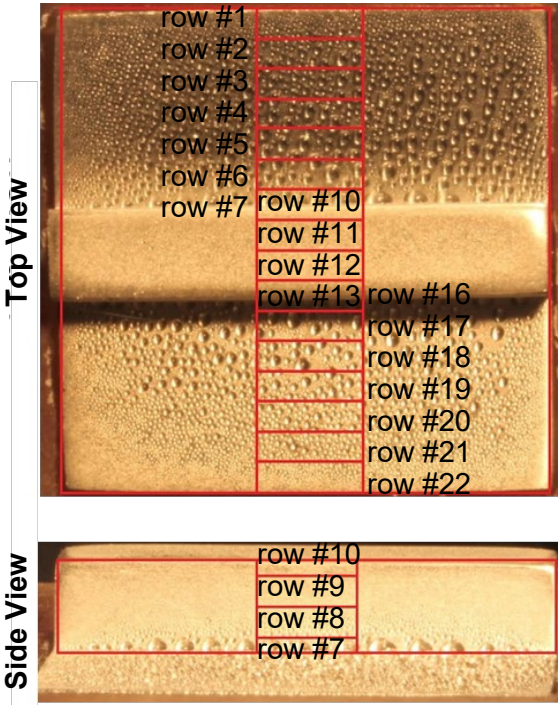
Figure 15. Division of the apparent area of the condensation block's top surface in the photograph for condensation rate analysis.

For each unit grid, we used a pixel-counting software to measure the radius R of each droplet with diameter larger than 2 pixels and summed up their volume, which can be calculated by:

$$V_{drop} = \pi R^3 (\frac{2}{3} - \cos\theta + \frac{\cos^3\theta}{3}),$$ (16)

where θ is the advancing contact angle. Then, the average heat flux in each row can be derived by integrating the condensation rate, the density and the latent heat of the water:

$$q = \frac{\sum V_{drop,t+\Delta t} - \sum V_{drop,t}}{A \cdot \Delta t} \cdot \rho \cdot h_{fg},$$ (17)

where q is the average heat flux of one row, t denotes the time; A is the surface area of one row; ρ and h_{fg} represent the density and the latent heat of the water, respectively.

Due to symmetry, we obtained the heat flux in rows 12-22 by directly mirroring the data for rows 1-11 along the symmetrical line. The image processing results are shown in Figure 16. Error bars indicate the propagation of error associated with the droplet diameter measurement (±1 pixel) during the image processing.
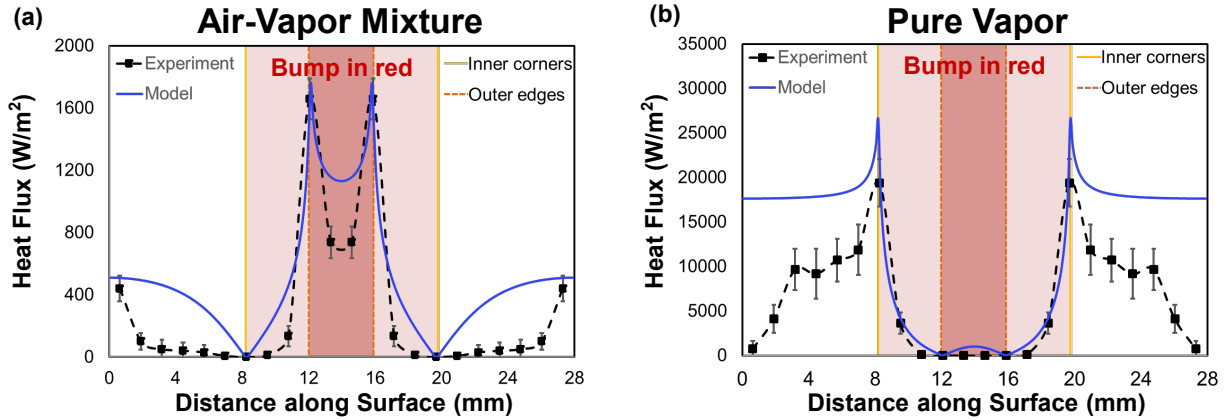
Figure 16. Condensation heat flux distribution along the top condenser surface in two cases: (a) condensation with air-vapor mixture, and (b) condensation with pure vapor, adapted from [62]. The bump region is highlighted in red with deep red for the top-surface region and light red for the sidewall region. Black data points are extracted from image processing on photographs taken from the experiments. Heat flux distribution derived from the numerical model is shown by the blue solid line.

Figure 16 (a) and (b) quantitatively show the condensation heat flux distribution along the top surface of the condensation block during the condensation experiments with air-vapor mixture and with pure vapor, respectively. The black data points were extracted from the images obtained during the two experiments by image processing. The blue solid lines show the heat flux distribution obtained from the numerical model. In the air-vapor mixture case, the maximum heat flux was reached at the outer edges of the bump, and there

was little heat flux at the inner corners, as shown in Figure 16 (a). However, in the pure vapor case, the outer edges had almost no heat flux, and the maximum heat flux was reached at the inner corners, as shown in Figure 16 (b). The completely different heat flux distribution in the two cases is mainly due to the different thermal resistance network altered by the presence of NCGs, as discussed. In both case studies, the experimental data and the modeling results show reasonable agreement with each other, especially the good agreement in the bump region and the similar trends in heat flux distribution. The discrepancy occurring at the flat regions was mainly due to the fact that in our experiment, we only used one bump and there was inevitable heat/mass dissipation on the vertical boundaries of the solid/gas regions, which differs from the assumption (3) we used in our modeling. Adding a heat flux dissipation term into the heat transfer equation in the pure vapor case model, or adding a mass flux dissipation term into the mass transfer equation in the air-vapor mixture case model, would mitigate this difference between the modeling and the experimental results. However, the focus of the current numerical modeling work is to build a general model to illustrate the effects of geometric features on condensation heat transfer under different vapor conditions. Modeling the heat dissipations from the boundaries could deviate the focus of the current study. Therefore, we did not revise the model to compensate for the inevitable heat dissipation occurred in the experiments. Despite the discrepancy in the flat regions, the reasonable agreement in heat flux distribution profile between experimental and modeling results demonstrates that the effects of the geometric features on dropwise condensation are not only determined by the geometric features themselves, but also significantly influenced by the vapor condition, which is capable of completely altering the thermal resistance network involved in the heat and mass transfer process. Based on our understanding, the condensation profile is determined by the overall thermal resistance network which is affected by many factors including the geometry of the condensation substrate, the material of the condensation substrate, and the vapor condition, rather than dependent on any one of these factors alone.

It is also worth noting that the heat flux obtained in the pure vapor condensation was generally much higher than the one obtained in the air-vapor mixture condensation. Averaging the local heat flux data along the block surface gave an average heat flux of 401±20 W/m^2 for the air-vapor mixture case study and 8676±551W/m^2 for the pure vapor case study. Direct comparison between the two heat flux values is not meaningful since they were measured at different degrees of subcooling, $\Delta T = (T_\infty - T_s)$. However, seeing that the heat flux value in the pure vapor case was over 20 times larger than that in the air-vapor mixture case, and that the subcooling in the pure vapor case was maintained at almost 0 °C which was much smaller than that in the air-vapor mixture case, from a scaling perspective, we can infer that the heat transfer coefficient, which is the ratio of the heat flux to the subcooling, has a much larger value in the pure vapor case than in

the air-vapor mixture case. Therefore, the NCGs in the air-vapor mixture case significantly degrade condensation heat transfer.

2.2.3 EXPERIMENTAL VALIDATION OF TEMPERATURE PROFILE ASSUMPTION

In the numerical modeling, based on thermal resistance analysis for the two cases, we made the approximation that the top surface temperature of the sample block T_s equaled to the bottom temperature of the block T_b in the air-vapor mixture case and to the saturation temperature of the bulk vapor T_∞ in the pure vapor case. We validated this approximation through direct temperature measurement for the two case studies.

In order to obtain the temperature profile on the top surface of the block, we attached three 36 gage (AWG, 0.13 mm in diameter) thermocouples at three different locations on the top surface of the block: (1) on the edge of the flat region; (2) on the top surface of the bump; and (3) on the sidewall of the bump. The thermocouples were attached to the surface using silver epoxy and cured for over 24 hours to ensure stable attachment to the block surface before the experiments. All thermocouples were calibrated by an Ultra Precise RTD Sensor (Omega) in a temperature-controlled water bath (Lauda RE 207) before use. The updated experimental configuration is shown in Figure 17.
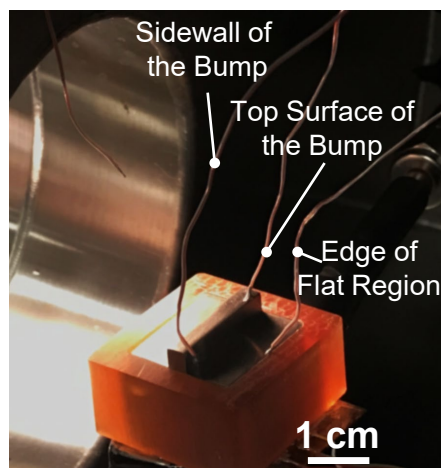
Figure 17. Three thermocouples were attached at different locations on the top surface of the block for direct temperature measurement.

Similar experimental conditions as those in the initial experiments for the two case studies were achieved when condensation occurred. During the condensation process, the surface temperature of the block T_s was recorded at the three different locations: the edge of the flat region (denoted by $T_{s,f}$), the top surface of the bump (denoted by $T_{s,t}$) and the sidewall of the bump (denoted by $T_{s,s}$).

In the case of air-vapor mixture condensation, the steady state condition was obtained at a bulk fluid temperature of 54.3°C with a relative humidity of 85%. For the pure vapor condensation, a steady state at vapor pressure of 5.9 kPa was maintained. The average values from direct temperature measurements for the two cases are listed in Table 2.

Table 2. Experimental conditions and direct temperature measurements

Case	T_∞ (°C)	Pressure (kPa)	RH(%)	T_b (°C)	$T_{s,f}$ (°C)	$T_{s,t}$ (°C)	$T_{s,s}$ (°C)
Air-Vapor Mixture	54.3	101.3	85.0	12.4	15.3	16.9	16.4
Pure Vapor	35.8	5.9	100.0	22.5	33.9	35.4	35.4

In both cases, the temperature measurement results agree with our model's assumption that the surface temperature of the block T_s should be much closer to the temperature of the element of the thermal resistance network with the much lower resistance (i.e., $(T_s-T_b)<<(T_\infty-T_s)$ in the air-vapor mixture case, where the thermal resistance of the air-vapor mixture dominates, and $(T_s-T_b)>>(T_\infty-T_s)$ in the pure vapor case, where the thermal resistance of the block dominates). In particular, for the pure vapor case, all of the temperatures on the surface of the block were measured to be almost the same as the temperature of the saturated vapor inside the chamber T_∞. This observation validated our approximation that $T_s \approx T_\infty$ in the pure vapor case. For the air-vapor mixture case, the direct measurement results show that there was a temperature difference of ~4°C between T_s and T_b, which could be attributed to two causes. First, the thermocouple measuring T_b was not in perfect contact with the bottom of the block due to the inevitable thermal resistance of the copper tape and the interfacial effects; therefore, the real value of T_b would be higher than the measured value. Second, the conduction and convection effects could decrease the thermal resistance on the gas region side, though these effects were small and thus neglected in our model. Although there was a small temperature change throughout the block, this value was less than one tenth of the

temperature difference between the block and the bulk fluid temperature (T_∞-T_s). Therefore, our approximation that $T_s \approx T_b$ in the air-vapor mixture case was justified.

2.3   ADDITIONAL CASE STUDY

Our work described in previous sections mainly focused on two extreme situations where the thermal resistance network is dominated by one side (either the gas region or the solid region). This great contrast in thermal resistance of the two regions enabled us to approximate the side with negligible resistance to be isothermal (assumptions (4) and (5)) and simplified our numerical modeling. However, it is also interesting to consider more complicated situations where some of the simplifications or assumptions are not valid anymore. For example, in the case where the thermal conductivity of the condensation substrate is so low that the thermal resistance of the substrate is comparable to that of the air-vapor mixture above the substrate, it is no longer feasible to approximate the substrate surface as isothermal. Nevertheless, it is still applicable to carry out a comprehensive thermal resistance analysis to obtain condensation profile, as long as careful consideration is taken into the energy balance among conduction heat flux of the substrate, latent heat flux released by condensation, and conduction heat flux of the air-vapor mixture (when convection is neglected).

In this section, we extend our discussion onto more complex thermal resistance scenarios. In order to demonstrate the applicability of the thermal resistance analysis, we exemplify a case study where we are able to predict the condensation profile through analysis of the thermal resistance network. Our prediction is then validated by numerical calculation results obtained from COMSOL Multiphysics [68].

For this case study, the geometry of the condensation substrate is the same as shown in Figure 7, but the substrate material is changed from titanium to another material with a low thermal conductivity of k=0.125 W/(mK), such that the thermal resistance of the geometric feature (δ / k) is estimated to be on the same order of magnitude as the thermal resistance of the air-vapor mixture ($1/h$) according to the literature [40, 61]. Therefore, it is no longer valid to assume the condensation substrate is isothermal and to obtain the condensation heat flux by simply solving the concentration profile in the gas region, as we did in the previous air-vapor mixture condensation case study presented in the main text.

The same boundary conditions as the previously considered air-vapor mixture case study are applied: (i) the bottom surface temperature of the condensation block is maintained at a constant T_b=12°C; (ii) the vapor temperature and relative humidity outside the diffusion boundary layer are kept at 56°C and 80%,

respectively; and (iii) adiabatic boundary conditions (no heat transfer or mass transfer in the horizontal direction) are applied to the two vertical boundaries of the considered 2D region.

Although it is no longer valid to assume the condensation block to be isothermal, the temperature variation on the top surface of the block is assumed to be small. Therefore, we can still utilize the shape factor method to calculate the diffusion boundary layer thickness, which yields the same thickness of 1 cm as calculated previously, since the shape factor method only depends on geometry. Preliminary prediction of the condensation profile can be made by comparing the thermal resistance involved in the characteristic solid region and gas region, as shown in Figure 18.
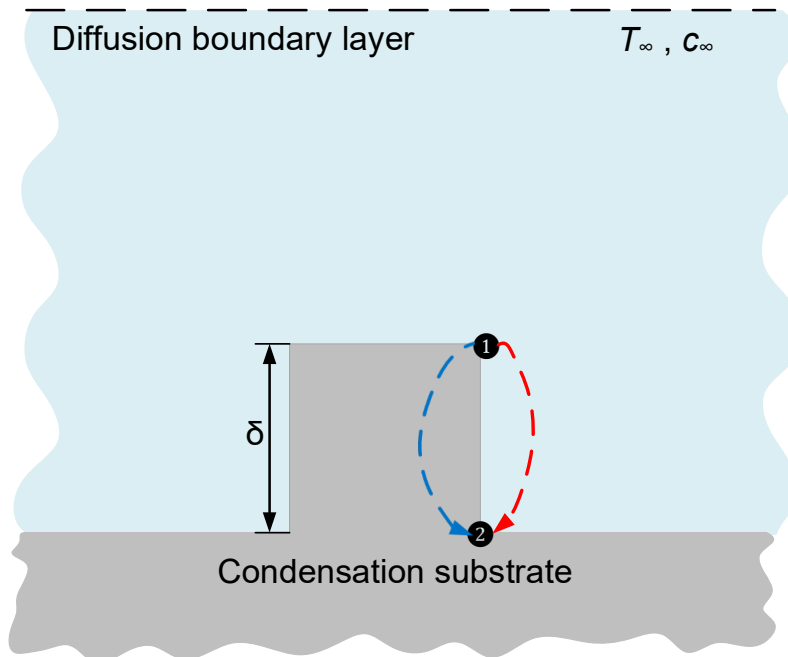
Figure 18. Schematic of the heat and mass transfer process occurring around the millimetric geometric feature.

When the heat of the air-vapor mixture reaches position 1, it has two routes to transfer to position 2: (1) through conduction in the solid region, as depicted by the blue dashed line; (2) through mass diffusion and conduction in the gas region, as depicted by the red dashed line. The preferred option of its travel route is determined by the thermal resistance network. For the conduction inside the solid (route (1)), the thermal resistance can be calculated by

$$R_{\text{th, solid}} = \delta / k_{\text{solid}}.$$

(18)

where k_{solid} is the thermal conductivity of the solid substrate (0.125 W/mK).

For the heat and mass transfer in the gas region (route (2)), the total thermal resistance can be calculated by its two paralleled components:

$$R_{th,\,gas} = 1/(1/R_{th,diff} + 1/R_{th,cond}) .\tag{19}$$

The first component of the resistance in Equation (19) accounts for the mass diffusion process, through which latent heat is released at the surface of the substrate:

$$\left| q \right| = \left| j \cdot M \cdot h_{fg} \right| = \left| D \cdot \frac{\Delta c}{\delta} \cdot M \cdot h_{fg} \right| ,\tag{20}$$

where M denotes the molar mass of water vapor (0.018 kg/mol), D is the diffusion coefficient of vapor in air ($\sim$3.0E-5 m^2/s), h_{fg} is the latent heat of water vapor ($\sim$ 2.4E6 J/kg) and Δc represents the concentration difference from position 1 to position 2.

According to the definition of thermal resistance per unit area:

$$R_{th} = \Delta T / q ,\tag{21}$$

the thermal resistance caused by the mass diffusion process can be determined as

$$R_{th,diff} = \Delta T / q = \frac{\Delta T}{D \cdot \dfrac{\Delta c}{\delta} \cdot M \cdot h_{fg}} = \frac{\Delta T}{D M h_{fg} \Delta c} \cdot \delta ,\tag{22}$$

where ΔT represents the temperature difference between position 1 and position 2.

The second component in Equation (19) represents the thermal resistance due to the conduction effects of the air-vapor mixture, which can be calculated by

$$R_{th,cond} = \delta / k_{gas} ,\tag{23}$$

where k_{gas} denotes the thermal conductivity of the humid air ($\sim$0.026 W/mK [37, 69]).

Combining Equations (18-23), we can derive the ratio of the thermal resistance of the two routes, denoted by the dimensionless number N:

$$N = \frac{R_{th,diff}}{R_{th,cond}} = \frac{(k_{gas} + \frac{DMh_{fg}\Delta c}{\Delta T})^{-1} \cdot \delta}{\frac{1}{k_{solid}} \cdot \delta} = \frac{k_{solid}}{k_{gas} + \frac{DMh_{fg}\Delta c}{\Delta T}}. \tag{24}$$

Based on the dimensionless number N, we can determine the condensation profile in general air-vapor mixture cases. If $N \gg 1$, water vapor would preferably condense on the outer edges of geometric features; if $N \ll 1$, condensation would more likely happen in the inner corners of the features. Note that this dimensionless number is not applicable to the case of pure vapor condensation situation since Fick's law is not valid for transport of concentrated species.

For the current case study, although the temperature and the corresponding concentration at positions 1 and 2 are unknown, one can derive through a simple scaling that in the considered situation, the value of $\Delta T/\Delta c$ for water near room temperature is on the order of 10. Substituting the values of all of the variables into Equation (24) yields $N \approx 1$, which predicts that heat has no preference for which route to travel, i.e., heat will transfer from the gas region into the substrate as if the two are the same media. Therefore, the isothermal and iso-concentration lines should be a series of horizontal lines. Consequently, condensation heat flux will almost be the same on the flat regions and the top surface of the bump, since the temperature gradient or concentration gradient in the vertical direction should almost be the same everywhere. However, there will be practically no condensation occurring on the sidewalls of the bump because the concentration gradient or the temperature gradient in the horizontal direction should almost be zero.

In order to demonstrate our prediction from the thermal resistance analysis, we solved the concentration profile in the gas region and the coupled temperature profile in the solid region simultaneously using the COMSOL Multiphysics program. The same boundary conditions at the bottom surface of the substrate and the gas region beyond the diffusion boundary layer as previously mentioned are applied. At the interface of the solid region and the gas region, the conduction heat flux of the solid is balanced by the sum of the conduction heat flux of the humid air and the latent heat flux released by the condensation of the water vapor. Numerical calculation results for the concentration and temperature distribution is shown in Figure 19. Furthermore, the condensation heat flux distribution along the top surface of the condensation substrate is derived from the concentration profile, as shown in Figure 20.
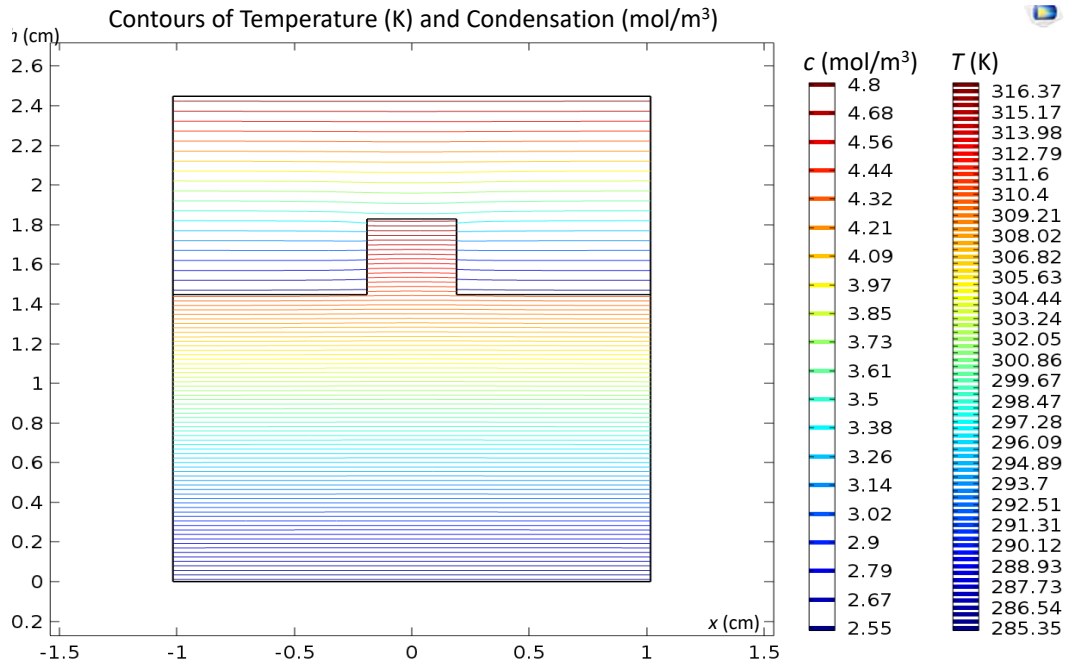
Figure 19. Concentration profile and temperature profile calculated by COMSOL Multiphysics.
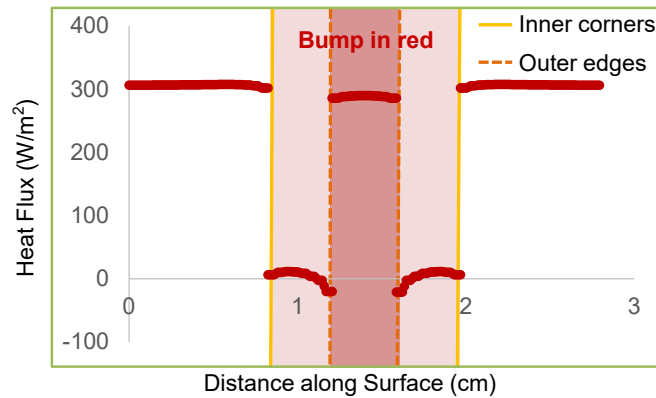
Figure 20. Condensation heat flux distribution along the top surface of the condenser calculated by COMSOL Multiphysics.

The calculation results for temperature profile, condensation profile and heat flux distribution obtained in COMSOL Multiphysics are in good agreements with our prediction from the thermal resistance analysis, which demonstrates that the predictive power of the thermal resistance analysis is not only suitable for simple case studies which we experimentally explored in the previous sections, but also offers useful insights to more complicated situations where multiple dominant factors are involved in the thermal resistance network.

45

Chapter 3

3. Dropwise Condensation of Low Surface Tension Fluids on Lubricant Infused Surfaces

3.1 DESIGN GUIDELINE FOR LIS

The design of lubricant infused surfaces (LIS) has been recently developed in terms of surface energies [59]. In the ideal case, the impinging fluids or condensates form discrete droplets resting atop the combined lubricant-solid layer of LIS and the lubricant remains trapped within the rough solid structured surface underneath, as shown in Figure 21.
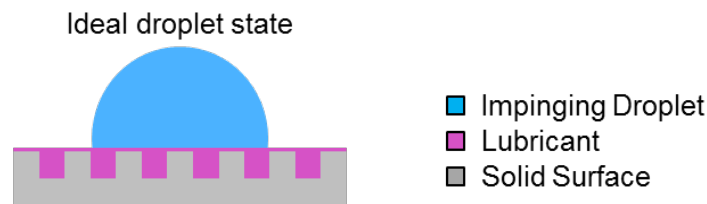
Figure 21. Successful design of lubricant infused surfaces.

Typical undesirable or failure modes of LIS can be summarized into five categories:

(I)   The lubricant spontaneously spreads over and "cloaks" the droplet, which does not belong to a failure mode but is undesirable considering the depletion of lubricants due to the "cloaking" effects;

(II)   The impinging fluid or condensates indefinitely spreads over the lubricant, resulting in formation of a film instead of discrete droplets (failure);

(III)   The lubricant does not spread within the rough structured solid surface in the presence of the vapor of the impinging fluid or condensate (failure);

(IV)   The lubricant does not spread within the rough structured solid surface in the presence of the liquid of the impinging fluid or condensate (failure);

(V)   The impinging fluid is miscible with the lubricant (failure).

Schematics of the five undesirable or failure modes of LIS design are shown in Table 3. For each of these undesirable or failure modes, certain energy criterion related to both the surface geometry and the material properties of the LIS, needs to be satisfied in order to avoid the corresponding undesirable/failure working
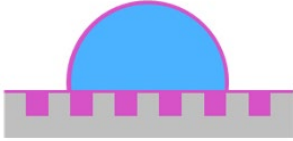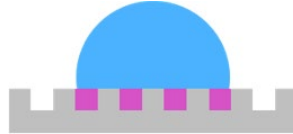
condition. The surface geometry of the solid substrate is described by the roughness, r, which represents the actual solid surface area divided by the projected area; and the solid fraction, φ, which represents the fraction of the solid which contacts the base of an impinging droplet. Combining the effects of these two parameters yields a comprehensive geometric factor $R = (r - 1)/(r - \varphi)$, which is an important parameter characterizing the surface geometry of LIS. The material properties of the LIS are represented by surface energies of phases with the surroundings (γ_A), and interfacial energies between different phases (γ_{AB}), involved in the system. Both γ_A and γ_{AB} can be obtained from the statistical thermodynamic model of van Oss, Chaudhury, and Good (vOCG) [59, 70]:

$$\gamma_A = \gamma_A^{LW} + 2\sqrt{\gamma_A^+\gamma_A^-}\ ; \tag{25}$$

$$\gamma_{AB} = \gamma_A^{LW} + \gamma_B^{LW} - 2\sqrt{\gamma_A^{LW}\gamma_B^{LW}} + 2\sqrt{\gamma_A^+\gamma_A^-} + 2\sqrt{\gamma_B^+\gamma_B^-} - 2\sqrt{\gamma_A^+\gamma_B^-} - 2\sqrt{\gamma_B^+\gamma_A^-}\ . \tag{26}$$

Subsequently, the spreading parameter $S_{AB} = \gamma_B - (\gamma_A + \gamma_{AB})$ for each interface in the system can be calculated, where the first and second subscripts refer to the spreading phase and the reference phase, respectively. Both the geometric factor R and the spreading parameter S_{AB} play important role in the design guideline to predict the LIS behavior. Detailed design guidelines regarding the five undesirable/failure modes are shown in Table 3, where the subscripts l, s, c and (c) correspond to lubricant, solid, condensate and the presence of condensate liquid, respectively.

Table 3. Undesirable or failure modes of LIS and corresponding design guidelines

Undesirable/Failure Conditions	Schematics	Design Guideline [59]
(I) The lubricant spontaneously spreads over and "cloaks" the droplet. (Undesirable)		$S_{lc} < 0$
(II) The impinging fluid spreads indefinitely over the lubricant, resulting in formation of a film instead of discrete droplets. (Failure)		$S_{cl} < 0$
(III) The lubricant does not spread within the rough structured solid surface in the presence of condensate vapor. (Failure)		$S_{ls} > -\gamma_l R$

		$S_{ls(c)} > -\gamma_{cl}R$

(IV) The lubricant does not spread within the rough structured solid surface in the presence of condensate liquid. (Failure)
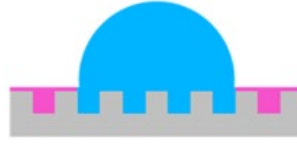
(V) The impinging fluid is miscible with the lubricant. (Failure)

$\gamma_{dl} > 0$

For the present work, an extremely low surface tension fluid, i.e., butane ($\gamma \approx 13$ mN/m), was used as the condensate to demonstrate the dropwise condensation behavior on LIS. According to the design guideline, dropwise condensation of butane on LIS is promising on the basis of proper combination of structured solid and lubricant. Previous study has experimentally shown that the combination of SiO$_2$ micro-pillars (with R = 0.71) as solid substrate and hexafluoroisopropanol (6F-IPA) as lubricant would yield a success LIS design that could repel impinging butane droplets [59]. The surface energy of each component in this designed LIS and the corresponding calculation results for the five design guidelines are shown in Table 4, which indicates that the same LIS design is capable of achieving dropwise condensation.

Table 4. Surface energy components [59] and design guideline calculations for the combination of SiO$_2$ micropillars (with R = 0.71) infused with hexafluoroisopropanol (6F-IPA) for butane condensation

Condensate	Lubricant	Structured Solid	Design Guidelines (satisfied if < 0)				
			(I)	(II)	(III)	(IV)	(V)
butane	6F-IPA	SiO$_2$ micropillars	S_{lc}	S_{cl}	$-(S_{ls}+\gamma_l R)$	$-(S_{ls(c)}+\gamma_{cl}R)$	$-\gamma_{dl}$
$\gamma = 12.5$ mN/m	$\gamma = 14.7$ mN/m	$\gamma = 59.8$ mN/m					
$\gamma^{LW} = 12.5$ mN/m	$\gamma^{LW} = 10.4$ mN/m	$\gamma^{LW} = 42.0$ mN/m	-6.2 mN/m	-2.2 mN/m	-50.3 mN/m	-19.7 mN/m	-4.2 mN/m
$\gamma^+ = 0.0$ mN/m	$\gamma^+ = 0.06$ mN/m	$\gamma^+ = 2.0$ mN/m					
$\gamma^- = 0.0$ mN/m	$\gamma^- = 70.0$ mN/m	$\gamma^- = 40.2$ mN/m					

Based on the LIS design guideline, we used the same combination of lubricant and solid substrate, namely 6F-IPA and SiO_2 micro-pillared structured surface (R=0.71) as a designed LIS for butane condensation experiments. Figure 22 shows the experimental setup for the demonstration of dropwise condensation of butane on the designed lubricant infused surfaces.
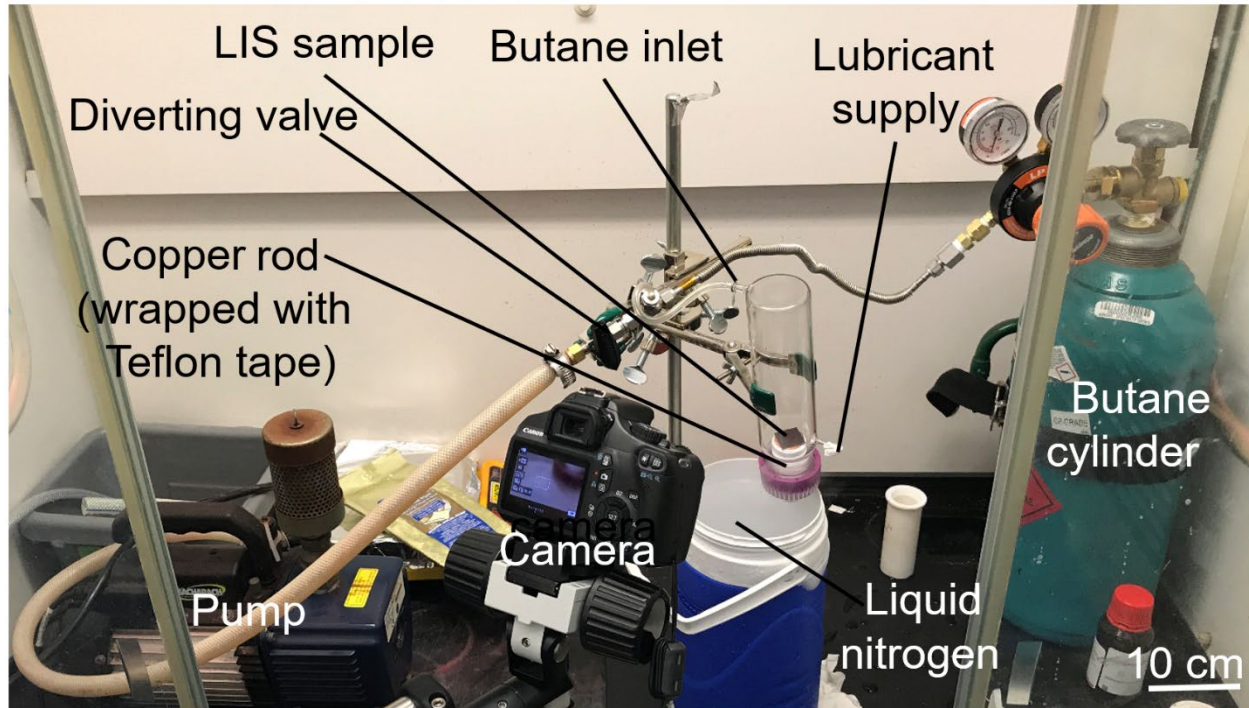
Figure 22. Experimental setup for demonstration of butane dropwise condensation on LIS.

Chemically-pure grade butane vapour (Airgas, purity 99.0%) was supplied from a butane cylinder to a customized glass vial (G. Finkenbeiner Inc.) through the butane inlet port. Next to the butane inlet port, a diverting valve was installed between the butane inflow line and the pump line that was connected to a vacuum pump. When the diverting valve was closed, the butane inlet port was only connected to the butane cylinder and the butane inflow rate was controlled by the pressure regulator on the butane cylinder. When the diverting valve was opened and the pressure regulator on the butane cylinder was closed, the vacuum pump pulled gases away and generated vacuum in the glass vial. A cylindrical copper rod was installed into the glass vial through the vial's cap and served as a condenser to transfer heat from its top surface (where the LIS sample was attached) to its bottom surface (which was exposed to liquid nitrogen). The sidewall of the copper rod was wrapped with Teflon tape for thermal insulation to prevent condensation on the side. LIS substrate, i.e. SiO_2-coated silicon micro-pillared surface, was rinsed with acetone, ethanol, IPA and DI water and plasma-cleaned with argon for 20 minutes before being attached to the copper condenser with

copper tape. Lubricant, i.e. 6F-IPA, could be supplied continuously by an injection syringe through another inlet port on the glass vial. All the interfaces between the glass vial and the outside environment were covered with Teflon tape to reduce invasion of non-condensable gases. A digital SLR camera (EOS Rebel T3, Canon) was installed facing the LIS sample to record images.

A set of procedures were followed throughout the experiment. The first step was to cool down the copper rod condenser by bringing its bottom surface in contact with liquid nitrogen (temperature of liquid nitrogen ≈ -195 °C). Meanwhile, we opened the diverting valve to the pump line to pull vacuum in the glass vessel. This procedure took less than a few minutes since the volume of the glass vessel was small. Then, we closed the diverting valve to the pump line, and infused lubricant (6F-IPA) onto the LIS sample surface through the lubricant supply port. The lubricant immediately wicked into the structured SiO_2 surface due to the strong polar interaction between the lubricant and the solid. Next, we open the pressure regulator on the butane cylinder to introduce butane vapor into the glass vessel. When butane vapor reached the cold LIS sample surface, condensation occurred and was recorded by the camera.

3.3   EXPERIMENTAL RESULTS

During the condensation experiment, we observed continuous generation of discrete butane droplets on the condenser surface, as shown in Figure 23. Therefore, we successfully demonstrated dropwise condensation of butane on the designed lubricant infused surface. Note that this is the first experimental demonstration of condensation in the dropwise mode for extremely low surface tension butane ($\gamma \approx 13$ mN/m).

Figure 23. Dropwise condensation of butane on 6F-IPA infused SiO_2 micro-pillared surface.

Even more interesting is the transition from filmwise condensation to dropwise condensation after infusing 6F-IPA on the originally bare SiO_2 micro-pillared surface. Figure 24 shows time lapse images of the transition behavior. At the beginning, butane was condensed on the bare SiO_2 micro-pillared structured surface, forming a layer of liquid film spreading over the structured solid substrate (Figure 24(a)), indicating that filmwise condensation was occurring on the bare structured solid substrate. Then, 6F-IPA was introduced from a needle of a syringe through the lubricant supply port on the glass vial, as shown in Figure 24(b). With the supply of the lubricant, we observed that the original liquid film of butane condensates covering the structured solid surface was displaced by the lubricant (Figures 24 (c)-(e)), which is in good agreement with the calculation result for LIS guideline (IV) in section 3.2. After removing the lubricant supply, the lubricant was able to adhere to the solid structured surface and kept promoting dropwise condensation of butane on the LIS for several minutes after which the lubricants would be depleted away, resulting in degradation and transition to filmwise condensation.
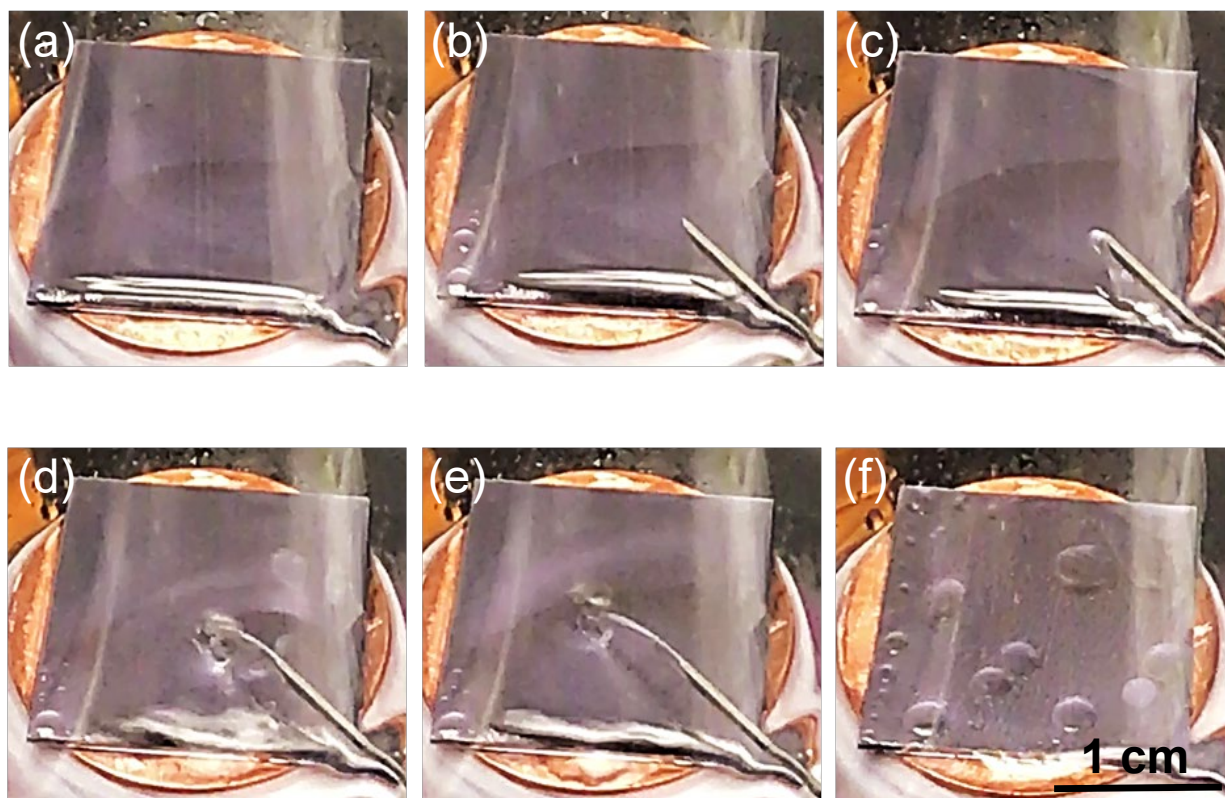
Figure 24. Transition of condensation modes on the same SiO_2 micro-pillared substrate after infusing 6F-IPA as lubricant. (a) Condensation of butane on bare SiO_2 micro-pillared structured surface, where butane completely wets the surface. (b) Introduction of the syringe to supply 6F-IPA as lubricant to the SiO_2 micro-pillared surface. (c) – (e) Addition of the lubricant *via* syringe showing displacement of condensed butane by the lubricant. (f) Shedding of condensed butane droplets on the 6F-IPA infused SiO_2 micro-pillared surface.

3.4 DISCUSSIONS ON HEAT TRANSFER MEASUREMENTS

In the previous section, we successfully demonstrated dropwise condensation of butane on the 6F-IPA infused SiO_2 surface, which shed light on promising enhancement in condensation heat transfer. Heat transfer measurements of butane condensation on the designed LIS were set up in an environmental chamber where the amount of non-condensable gases could be well controlled. However, it was challenging to perform the heat transfer measurements due to the volatile nature of the lubricant we used. 6F-IPA has a relatively higher vapor pressure (~16 Kpa at 20 ºC) and evaporates away easily. During the experiments, a fast depletion rate of the lubricant was observed even before condensation of butane occurred.

In order to keep the SiO_2 substrate constantly infused with 6F-IPA, we tried to use a customized glass vial with two ports as a lubricant reservoir to keep dripping 6F-IPA onto the SiO_2 surface throughout the heat transfer experiments. The dripping method worked well for the purpose of adding lubricant continuously, but the dripping rate and the dripping time were not under good control. Once we closed the chamber door, the reservoir started dripping lubricants and kept the LIS functional for around 30 minutes after which all the lubricants in the glass vial were gone. We were not able to achieve steady state condensation before running out of lubricants, so no heat transfer measurement data were reported in the present work.

In addition to the difficulty of controllably adding 6F-IPA into the system, the evaporation of 6F-IPA also poses a challenge to the heat transfer measurements. Normally, we extrapolate the condensation heat flux from the 1D conduction heat flux measured by an array of thermocouples inserted in the condenser underneath the sample, assuming that all the latent heat released from condensation is transferred to the back of the condenser through 1D conduction. However, when there is a considerable amount of evaporation occurring simultaneously on the sample surface, the 1D conduction heat flux measured from the condenser would underestimate the actual condensation heat transfer performance. It would be helpful to do a scaling comparison between the condensation heat flux and the evaporation heat flux. The latent heat of 6F-IPA (~2.5×10^5 J/kg) and of butane (~3.6×10^5 J/kg) are on the same order of magnitude. Therefore, the significance of the evaporation effects is determined by the mass flux of the lubricant leaving the surface. Nevertheless, there is no information we could find about diffusion coefficient of 6F-IPA in butane vapor, which retrained us from obtaining a reliable scaling argument for the evaporation heat flux.

Considering that the volatile nature of 6F-IPA brings various challenges and complexities to the heat transfer experiments, we have been looking for other lubricants including Krytox GPL 100 oil that could possibly work for dropwise condensation of butane, under the guidance of the LIS model developed in previous work [59]. However, no substitute for 6F-IPA has been found yet as of the writing of this thesis.

Chapter 4

4. Summary and Future Directions

4.1 DROPWISE CONDENSATION OF WATER ON MILLIMETRIC GEOMETRIC FEATURES

We investigated dropwise condensation of water on millimetric structured surface, both with and without the presence of non-condensable gases. Based on the analysis of the thermal resistance network, numerical models were developed for condensation heat flux distribution in the two cases. Meanwhile, droplet growth rate was experimentally captured and converted to heat flux through image processing. The good agreement between modeling and experimental results demonstrates that the same convex geometric feature, or bump, can impose opposite effects on dropwise condensation of water under different vapor conditions. Based on our analysis, the effects of geometric features on dropwise condensation are not absolute, but rather depend on the thermal resistances involved in the system. Moreover, the predictive power of the thermal resistance network analysis was demonstrated through an additional case study where more complicated thermal resistances were involved.

The focus of this work mainly lies in two extreme cases where the thermal resistance network is dominated by only one region, i.e. the vapor-dominated thermal resistance network in the air-vapor case or the solid-dominated thermal resistant network in the pure vapor case. However, it would be also interesting to experimentally explore some other scenarios where multiple thermal resistances are involved, for instance, a transition case where the gas region has equivalent thermal resistance to the solid region.

Degradation of condensation heat transfer performance caused by non-condensable gases has been shown in the present study, but the content or mass ratio of the non-condensable gases was not well controlled. In the future, it would be helpful to quantitively investigate how different contents of non-condensable gases would affect the dropwise condensation of water on structured surfaces.

Furthermore, current work considers the effects of only one millimetric geometric feature, i.e., a rectangular bump, on the dropwise condensation of water. How different structure shapes or numbers of the millimetric structures on the condenser surface could affect the dropwise condensation performance would be an interesting direction to explore.

4.2 DROPWISE CONDENSATION OF LOW SURFACE TENSION FLUIDS ON LUBRICANT INFUSED SURFACES

Based on a recently developed design guideline for lubricant infused surfaces (LIS), we successfully demonstrated dropwise condensation of an extremely low surface tension fluid, i.e., butane, on a specifically designed lubricant infused surface composed of SiO_2 micro-pillared structured solid and hexafluoroisopropanol (6F-IPA) lubricant. This is the first experimental demonstration of condensation in the dropwise mode with a condensate with such a low surface tension ($\gamma \approx 13$ mN/m).

Dropwise condensation of butane shown in the current study promises an enhancement in heat transfer performance as compared to conventional filmwise condensation. Future work entails quantitative heat transfer measurement of dropwise condensation with butane on LIS.

Lubricant depletion rate plays a critical role in the robustness of LIS. Multiple factors contribute to lubricant depletion, such as shear force introduced by the shedding droplets, evaporation of the lubricant and "cloaking" effects. Although "cloaking" effects do not exist in the present study, a fast lubricant depletion rate has been observed during the experiments, which is probably owing to the evaporation effects. 6F-IPA is a volatile fluid (boiling temperature ≈ 58.2 °C under 1 bar) and therefore is easy to evaporate away from the LIS substrate, which poses a challenge for making a long-lasting LIS design for butane dropwise condensation. Research on other lubricants with better performance in longevity, or other solid substrates that can hold the lubricant for a longer time, is required for making an applicable and robust LIS design for condensing extremely low surface tension fluids such as butane. Variation of lubricant depletion rate with respect to different geometry of surface structures would be another insightful direction to explore.

The present study is mainly focused on butane, which is a typical example of low surface tension fluids and plays an important role in industrial applications such as natural gas processing. It would be also interesting to explore dropwise condensation on lubricant infused surfaces with other low surface tension fluids such as propane, which has an even lower surface tension ($\gamma \approx 8$ mN/m) as compared to butane and is an important product in natural gas processing and petroleum refining.

5. Bibliography

1. Hao, C., et al., *Bioinspired Interfacial Materials with Enhanced Drop Mobility: From Fundamentals to Multifunctional Applications.* Small, 2016. **12**(14): p. 1825-39.
2. Huang, Z., Y. Hwang, and R. Radermacher, *Review of nature-inspired heat exchanger.* International Journal of Refrigeration, 2017. **78**: p. 1-17.
3. Cho, H.J., et al., *Nanoengineered materials for liquid–vapour phase-change heat transfer.* Nature Reviews Materials, 2016. **2**: p. 16092.
4. Rifert, V.G., et al., *Heat-Exchange at Dropwise Condensation in Heat-Exchangers of Desalination Plants.* Desalination, 1989. **74**(1-3): p. 373-382.
5. Caruso, G., D. Vitale Di Maio, and A. Naviglio, *Condensation heat transfer coefficient with noncondensable gases inside near horizontal tubes.* Desalination, 2013. **309**: p. 247-253.
6. Preston, D.J., et al., *Scalable graphene coatings for enhanced condensation heat transfer.* Nano Lett, 2015. **15**(5): p. 2902-9.
7. D. A. McNeil, B.M.B.G.C., *Dropwise Condensation of Steam on a Small Tube Bundle at Turbine Condenser Conditions.* Experimental Heat Transfer, 2000. **13**(2): p. 89-105.
8. Park, K.C., et al., *Optimal design of permeable fiber network structures for fog harvesting.* Langmuir, 2013. **29**(43): p. 13269-77.
9. Kim, H., et al., *Water harvesting from air with metal-organic frameworks powered by natural sunlight.* Science, 2017. **356**(6336): p. 430-434.
10. Yadav, M.K., S. Khandekar, and P.K. Sharma, *An integrated approach to steam condensation studies inside reactor containments: A review.* Nuclear Engineering and Design, 2016. **300**: p. 181-209.
11. Kim, H., T.-S. Kwon, and D.E. Kim, *Experimental study of air-cooled water condensation in slightly inclined circular tube using infrared temperature measurement technique.* Nuclear Engineering and Design, 2016. **308**: p. 38-50.
12. Zhao, Y., et al., *Comprehensive analysis and parametric optimization of a CCP (combined cooling and power) system driven by geothermal source.* Energy, 2016. **97**: p. 470-487.
13. Traviss, D.P., *Condensation in refrigeration condensers*, in *Mechanical Engineering*. 1972, Massachusetts Institute of Technology.
14. Seader, J.D. and E.J. Henley, *Separation process principles*. 2nd ed. 2005: Wiley.
15. Ahmed, M.J. and M.S. Hussein, *Experimental and theoretical analysis of iso-butane recovery from linear paraffinic hydrocarbons by adsorption on 5A zeolite.* Journal of Natural Gas Science and Engineering, 2015. **27**: p. 763-768.
16. Rose, J.W., *dropwise condensation theory and experiment: a review.* Proceedings of the Institution of Mechanical Engineering, 2002. **216**: p. 115-128.
17. Schmidt, E., W. Schurig, and W. Sellschopp, *Versuche über die Kondensation von Wasserdampf in Film- und Tropfenform.* Technische Mechanik und Thermodynamik, 1930. **1**: p. 53-63.
18. Miljkovic, N., et al., *Jumping-droplet-enhanced condensation on scalable superhydrophobic nanostructured surfaces.* Nano Lett, 2013. **13**(1): p. 179-87.
19. Le Fevre, E.J. and J.W. Rose, *A theory of heat transfer by dropwise condensation.* Proc. Third Int. Heat Transfer Conf., 1966: p. 362-375.
20. Tanaka, H., *A theoretical study of Dropwise Condensation.* Transactions ASME J. Heat Transfer, 1975. **97**: p. 72-78.
21. Kim, S. and K.J. Kim, *Dropwise Condensation Modeling Suitable for Superhydrophobic Surfaces.* Journal of Heat Transfer, 2011. **133**(8): p. 081502.
22. Miljkovic, N., R. Enright, and E.N. Wang, *Modeling and Optimization of Superhydrophobic Condensation.* Journal of Heat Transfer, 2013. **135**(11): p. 111004.

23. Wen, R., et al., *Hydrophobic copper nanowires for enhancing condensation heat transfer.* Nano Energy, 2017. **33**: p. 177-183.
24. Mouterde, T., et al., *Antifogging abilities of model nanotextures.* Nat Mater, 2017.
25. Chen, C.-H., et al., *Dropwise condensation on superhydrophobic surfaces with two-tier roughness.* Applied Physics Letters, 2007. **90**(17): p. 173108.
26. Mandsberg, N.K. and R. Taboryski, *Spatial Control of Condensation on Chemically Homogeneous Pillar-Built Surfaces.* Langmuir, 2017.
27. Xie, J., et al., *Large scale generation of micro-droplet array by vapor condensation on mesh screen piece.* Sci Rep, 2017. **7**: p. 39932.
28. Varanasi, K.K., et al., *Spatial control in the heterogeneous nucleation of water.* Applied Physics Letters, 2009. **95**(9): p. 094101.
29. Preston, D.J., et al., *Electrowetting-on-Dielectric Actuation of a Vertical Translation and Angular Manipulation Stage.* Applied Physics Letters, 2016. **109**(24): p. 244102.
30. Nam, Y. and Y.S. Ju, *Comparative Study of Copper Oxidation Schemes and Their Effects on Surface Wettability.* Imece 2008: Heat Transfer, Fluid Flows, and Thermal Systems, Vol 10, Pts a-C, 2009: p. 1833-1838.
31. Miljkovic, N., et al., *Jumping-droplet electrostatic energy harvesting.* Applied Physics Letters, 2014. **105**(1).
32. Cavalli, A., et al., *Electrically induced drop detachment and ejection.* Physics of Fluids, 2016. **28**(2).
33. Preston, D.J., et al., *Jumping Droplet Electrostatic Charging and Effect on Vapor Drag.* Journal of Heat Transfer-Transactions of the Asme, 2014. **136**(8).
34. Miljkovic, N., et al., *Electrostatic charging of jumping droplets.* Nature Communications, 2013. **4**(2517).
35. Oh, J., et al., *Jumping-droplet electronics hot-spot cooling.* Applied Physics Letters, 2017. **110**(12).
36. Park, K.C., et al., *Condensation on slippery asymmetric bumps.* Nature, 2016. **531**(7592): p. 78-82.
37. Medici, M.G., et al., *Edge effects on water droplet condensation.* Phys Rev E Stat Nonlin Soft Matter Phys, 2014. **90**(6): p. 062403.
38. Zhu, A.M., et al., *Effects of high fractional noncondensable gas on condensation in the dewvaporation desalination process.* Desalination, 2007. **214**(1-3): p. 128-137.
39. Danilo, S., C. Dominique, and P. Frederic, *Experimental dropwise condensation of unsaturated humid air - Influence of humidity level on latent and convective heat transfer for fully developed turbulent flow.* International Journal of Heat and Mass Transfer, 2016. **102**: p. 846-855.
40. Chantana, C. and S. Kumar, *Experimental and theoretical investigation of air-steam condensation in a vertical tube at low inlet steam fractions.* Applied Thermal Engineering, 2013. **54**(2): p. 399-412.
41. Colburn, A.P. and O.A. Hougen, *Design of cooler condensers for mixtures of vapors with noncondensing gases.* Industrial and Engineering Chemistry, 1934. **26**: p. 1178-1182.
42. Minkowycz, W.J. and E.M. Sparrow, *Condensation heat transfer in the presence of noncondensables, interfacial resistance, superheating, variable properties, and diffusion.* Int. J. Heat Mass Transfer, 1966. **9**(10): p. 1125-1144.
43. Liao, Y. and K. Vierow, *A Generalized Diffusion Layer Model for Condensation of Vapor With Noncondensable Gases.* Journal of Heat Transfer, 2007. **129**(8): p. 988.
44. Huang, J., J. Zhang, and L. Wang, *Review of vapor condensation heat and mass transfer in the presence of non-condensable gas.* Applied Thermal Engineering, 2015. **89**: p. 469-484.
45. Othmer, F.F., *The Condensation of Steam.* Indus. Eng. Chem., 1929. **21**: p. 577-583.
46. Sparrow, E.M. and E.R.G. Eckert, *Effects of Superheated Vapor and Noncondensable Gases on Laminar Film Condensation.* Aiche Journal, 1961. **7**(3): p. 473-477.
47. Al-Shammari, S.B., D.R. Webb, and P. Heggs, *Condensation of steam with and without the presence of non-condensable gases in a vertical tube.* Desalination, 2004. **169**(2): p. 151-160.

48. Bum-Jin, C., et al., *Experimental comparison of film-wise and drop-wise condensations of steam on vertical flat plates with the presence of air.* International Communications in Heat and Mass Transfer, 2004. **31**(8): p. 1067-1074.

49. Al-Diwany, H.K. and J.W. Rose, *Free convection film condensation of steam in the presence of non-condensing gases.* Int. J. Heat Mass Transfer, 1973(16): p. 1359-1369.

50. Liu, T.L. and C.J. Kim, *Repellent surfaces. Turning a surface superrepellent even to completely wetting liquids.* Science, 2014. **346**(6213): p. 1096-100.

51. Weisensee, P.B., et al., *Hydrophobic and oleophobic re-entrant steel microstructures fabricated using micro electrical discharge machining.* Journal of Micromechanics and Microengineering, 2014. **24**(9): p. 095020.

52. Enright, R., et al., *Condensation on superhydrophobic surfaces: the role of local energy barriers and structure length scale.* Langmuir, 2012. **28**(40): p. 14424-32.

53. Lafuma, A. and D. Quéré, *Slippery pre-suffused surfaces.* EPL (Europhysics Letters), 2011. **96**(5): p. 56001.

54. Wong, T.S., et al., *Bioinspired self-repairing slippery surfaces with pressure-stable omniphobicity.* Nature, 2011. **477**(7365): p. 443-7.

55. Rykaczewski, K., et al., *Dropwise condensation of low surface tension fluids on omniphobic surfaces.* Sci Rep, 2014. **4**: p. 4158.

56. Preston, D.J., et al., *Heat Transfer Enhancement During Water and Hydrocarbon Condensation on Lubricant Infused Surfaces.* Sci Rep, 2018. **8**(1): p. 540.

57. Kajiya, T., et al., *3D Imaging of Water-Drop Condensation on Hydrophobic and Hydrophilic Lubricant-Impregnated Surfaces.* Sci Rep, 2016. **6**: p. 23687.

58. Weisensee, P.B., et al., *Condensate droplet size distribution on lubricant-infused surfaces.* International Journal of Heat and Mass Transfer, 2017. **109**: p. 187-199.

59. Preston, D.J., et al., *Design of Lubricant Infused Surfaces.* ACS Appl Mater Interfaces, 2017. **9**(48): p. 42383-42392.

60. Bahadori, A., *Natural gas processing : technology and engineering design.* 1st ed. 2014: Gulf Professional Publishing. 896.

61. Götze, P., C. Philipp, and U. Gross, *Dropwise Condensation Experiments with Humid Air at a Polymer Surface.* Journal of Physics: Conference Series, 2012. **395**: p. 012129.

62. Zhao, Y., et al., *Effects of millimetric geometric features on dropwise condensation under different vapor conditions.* International Journal of Heat and Mass Transfer, 2018. **119**: p. 931-938.

63. Smith, J.D., et al., *Hydrate-phobic surfaces: fundamental studies in clathrate hydrate adhesion reduction.* Phys Chem Chem Phys, 2012. **14**(17): p. 6013-20.

64. Vosough, A., et al., *Improvement Power Plant Efficiency with Condenser Pressure.* Int. J. Multidiscipl. Sci. Eng., 2011. **2**: p. 38-43.

65. Beysens, D., *Dew nucleation and growth.* Comptes Rendus Physique, 2006. **7**(9-10): p. 1082-1100.

66. Holman, J.P., *Heat Transfer.* 10 ed. 2009: McGraw-Hill Higher Education. 752.

67. Mills, A.F., *Mass Transfer.* 1 ed. 2001: Prentice Hall.

68. *https://www.comsol.com/comsol-multiphysics*.

69. Tsilingiris, P.T., *Thermophysical and transport properties of humid air at temperature range between 0 and 100°C.* Energy Conversion and Management, 2008. **49**(5): p. 1098-1110.

70. Sett, S., et al., *Lubricant-Infused Surfaces for Low-Surface-Tension Fluids: Promise versus Reality.* ACS Appl Mater Interfaces, 2017. **9**(41): p. 36400-36408.

Appendix

TFTS SURFACE FUNCTIONALIZATION

Trichloro(1H,1H,2H,2H-perfluorooctyl)silane (TFTS) was deposited onto the titanium block by the following procedures. Before silane deposition, the sample was rinsed with ethanol and DI water, and then oxygen plasma cleaned for 3 hours to remove organic contaminants on the surface. After clean, the titanium block was immediately placed into a solution made of 0.001Mol of TFTS in hexane. Then, the solution was heated up to 60 ºC using a hot plate and kept there for an hour with a stir bar placed within the solution. The top of the solution was covered with aluminum foil during the heating process to prevent evaporation. Afterwards, the titanium block was rinsed in ethanol and DI water, and dried at 120 ºC on a hot plate for another hour.

DROPWISE CONDENSATION OF WATER ON MILLIMETRIC GEOMETRIC FEATURES MATLAB CODE

PURE VAPOR CASE:

```
clc;clear all;close all;
x_length=0.8*2.54*0.01;
y_length=0.57*2.54*0.01;
h_length=0.15*2.54*0.01;
l_length=0.325*2.54*0.01;
w_length=0.15*2.54*0.01;
a=0.005*2.54*0.01;
n_x=round(x_length/a);
n_y=round(y_length/a);
n_h=round(h_length/a);
n_l=round(l_length/a);
n_w=round(w_length/a);
k=15.6;
k_ultem=0.122;
T_top=refpropm('T','P',6,'Q',0,'water');
T_bot=20+273.15;%%%temperature measured by thermal couple
[rho_water_vap] = refpropm('D','T',T_top,'Q',0,'water');
M_water= 0.01802;
c_water_vap=rho_water_vap/M_water;
% BC_top=255*ones(1,x_elements);
% BC_LHS=[0*ones(1,y_elements)]';
% BC_RHS=[0*ones(1,y_elements)]';
% BC_bot=0*ones(1,x_elements);

for ix=1:n_x,
    for iy=1:n_h+n_y-1,
        temp(iy,ix)=T_top;
    end
```

```matlab
end
BC_bot=T_bot*ones(1,n_x);
total_temp=[temp;BC_bot];
total_temp2=total_temp;

for j=1:30000;
for ix=1:n_l+1,
    for iy=2+n_h:n_h+n_y-1,
        if ix==1,
            total_temp2(iy,ix)=(total_temp((iy-
1),ix)+total_temp((iy+1),ix)+total_temp(iy,(ix+1)))/3;
        else
            total_temp2(iy,ix)=0.25*(total_temp(iy-
1,ix)+total_temp(iy+1,ix)+total_temp(iy,ix-1)+total_temp(iy,ix+1));
        end
    end
end
for ix=n_l+2:n_l+n_w-1;
    for iy=2:n_h+n_y-1;
        total_temp2(iy,ix)=0.25*(total_temp(iy-
1,ix)+total_temp(iy+1,ix)+total_temp(iy,ix-1)+total_temp(iy,ix+1));
    end
end
for ix=n_l+n_w:n_x,
    for iy=n_h+2:n_h+n_y-1;
        if ix==n_x,
        total_temp2(iy,ix)=(total_temp(iy-
1,ix)+total_temp(iy+1,ix)+total_temp(iy,ix-1))/3;
            else
            total_temp2(iy,ix)=0.25*(total_temp(iy-
1,ix)+total_temp(iy+1,ix)+total_temp(iy,ix-1)+total_temp(iy,ix+1));
        end
    end
end


total_temp=total_temp2;
converge(j)=total_temp(n_x/2,n_y/2);
end
% examine convergence
figure(1)
plot(converge)
set(figure(1),'Name','Convergence');
surface(total_temp(end:-1:1,:))
%plot heat flux along the surface line of the block
for i=1:n_x+n_h+n_h,
    if (i<=n_l),
        q(i)= k*(total_temp(n_h+1,i)-total_temp(n_h+2,i))/a;
    else if ((i>n_l)&&(i<n_l+n_h)),
            q(i)=k*(total_temp((n_l+n_h+1-i),(n_l+1))-total_temp((n_l+n_h+1-
i),(n_l+2)))/a;
    else if((i>(n_l+n_h+1))&&(i<(n_l+n_h+n_w))),
            q(i)=k*(total_temp(1,(i-n_h))-total_temp(2,(i-n_h)))/a;
        else if (i>(n_l+n_h+n_w))&&(i<=(n_l+n_h+n_w+n_h)),
                q(i)=k*(total_temp((i-n_l-n_h-n_w),(n_l+n_w))-total_temp((i-
n_l-n_h-n_w),(n_l+n_w-1)))/a;
        else if (i>=(n_l+n_w+n_h+n_h+1)),
```

```matlab
                q(i)=k*(total_temp(n_h+1,(i-n_h-n_h))-total_temp(n_h+2,(i-
n_h-n_h)))/a;
            else if
(i==n_l+n_h)||(i==n_l+n_h+1)||(i==n_l+n_h+n_w)||(i==n_l+n_h+n_w+1),
                    q(i)=0
                end
            end
            end
        end
        end
    end


end
Volume=0;
h_cool_bubble=refpropm('H','T',T_top,'Q',1,'water');
h_cool_dew=refpropm('H','T',T_top,'Q',0,'water');
h_fg=h_cool_bubble-h_cool_dew;
rho_water=refpropm('D','T',T_top,'Q',0,'water');
for i=1:n_x+n_h+n_h,
    jj(i)=i*a;
    Volume2=Volume+0.832*2.54*0.01*a*q(i)/h_fg/rho_water;
    Volume=Volume2;
end
figure(2)
plot(jj,q);
set(figure(2),'Name','Heat flux');

%transllate real temperature range to 0-255 range for visualization
for ix=1:n_x,
    for iy=1:n_h+n_y,
        total_temp3(iy,ix)=(total_temp(iy,ix)-T_bot)/(T_top-T_bot)*255;
    end
end
figure(3)
imshow(total_temp3,[0,255])
contour(total_temp,17)
```

AIR-VAPOR CASE:

```matlab
clc;clear all;close all;
x_length=2.54*0.01*0.8;
y_length=2.54*0.01*0.005*78;%%%m based on boundary layer thickness
h_length=0.15*2.54*0.01;
l_length=0.325*2.54*0.01;
w_length=0.15*2.54*0.01;
a=0.005*2.54*0.01;
n_x=round(x_length/a);
n_y=round(y_length/a);
n_h=round(h_length/a);
n_l=round(l_length/a);
n_w=round(w_length/a);
T_base = 12+273.15;%experimental data
T_vap = 55.8+273.15;%experimental data
dT = T_vap - T_base;
P_chamber=101;
```

```matlab
D=0.00003;%diffusion constant of water in air (m^2/s)
[Ps_base,rho_water_base] = refpropm('PD','T',T_base,'Q',1,'water');
[Ps_vap] = refpropm('P','T',T_vap,'Q',1,'water');
rh=0.90;%relative humidity
P_vap=Ps_vap*rh;
[rho_water_vap] = refpropm('D','T',T_vap,'P',P_vap,'water');
Ts_vap=refpropm('T','P',P_vap,'Q',1,'water')-273.15;
M_air=0.029;
M_water= 0.018;
c_water_base=rho_water_base/M_water;
c_water_vap=rho_water_vap/M_water;
c_top=c_water_vap;
c_bot=c_water_base;%temperature measured by thermal couple
% BC_top=255*ones(1,x_elements);
% BC_LHS=[0*ones(1,y_elements)]';
% BC_RHS=[0*ones(1,y_elements)]';
% BC_bot=0*ones(1,x_elements);

for ix=1:n_x,
    for iy=1:n_h+n_y-1,
        c(iy,ix)=c_bot;
    end
end
BC_top=c_top*ones(1,n_x);
total_c=[BC_top;c];
total_c2=total_c;

for j=1:30000;
for ix=1:n_l-1,
    for iy=2:n_h+n_y-1,
        if ix==1,
            total_c2(iy,ix)=(total_c((iy-
1),ix)+total_c((iy+1),ix)+total_c(iy,(ix+1)))/3;
        else
            total_c2(iy,ix)=0.25*(total_c(iy-
1,ix)+total_c(iy+1,ix)+total_c(iy,ix-1)+total_c(iy,ix+1));
        end
    end
end
for ix=n_l:n_l+n_w+1;
    for iy=2:n_y-1;
        total_c2(iy,ix)=0.25*(total_c(iy-
1,ix)+total_c(iy+1,ix)+total_c(iy,ix-1)+total_c(iy,ix+1));
    end
end
for ix=n_l+n_w+2:n_x,
    for iy=2:n_h+n_y-1;
        if ix==n_x,
        total_c2(iy,ix)=(total_c(iy-1,ix)+total_c(iy+1,ix)+total_c(iy,ix-
1))/3;
        else
            total_c2(iy,ix)=0.25*(total_c(iy-
1,ix)+total_c(iy+1,ix)+total_c(iy,ix-1)+total_c(iy,ix+1));
        end
    end
end
total_c=total_c2;
```

```matlab
        converge(j)=total_c(n_x/2,n_y/2);
    end

% examine convergence
figure(1)
plot(converge)
set(figure(1),'Name','Convergence');
%plot mass flux along the surface line of the block
for i=1:n_x+n_h+n_h,
    if (i<=n_l-1),
        J(i)= D*(total_c(n_h+n_y-1,i)-total_c(n_h+n_y,i))/a;
    else if ((i>n_l+1)&&(i<=n_l+n_h)),
            J(i)=D*(total_c((n_y+n_l+n_h+1-i),(n_l-1))-
total_c((n_y+n_l+n_h+1-i),n_l))/a;
        else if((i>(n_l+n_h))&&(i<=(n_l+n_h+n_w))),
            J(i)=D*(total_c(n_y-1,(i-n_h))-total_c(n_y,(i-n_h)))/a;
            else if (i>(n_l+n_h+n_w))&&(i<(n_l+n_h+n_w+n_h)),
                J(i)=D*(total_c((n_y+i-n_l-n_h-n_w),(n_l+n_w+2))-
total_c((n_y+i-n_l-n_h-n_w),(n_l+n_w+1)))/a;
            else if (i>(n_l+n_w+n_h+n_h+1)),
                J(i)=D*(total_c(n_y+n_h-1,(i-n_h-n_h))-total_c(n_y+n_h,(i-
n_h-n_h)))/a;
                else if
(i==n_l)||(i==n_l+1)||(i==n_l+n_h+n_h+n_w)||(i==n_l+n_h+n_h+n_w+1),
                    J(i)=0
                    end
                end
            end
        end
        end
    end

end
rho_water=refpropm('D','P',Ps_base,'Q',0,'water');
h_cool_bubble=refpropm('H','P',Ps_base,'Q',1,'water');
h_cool_dew=refpropm('H','P',Ps_base,'Q',0,'water');
h_fg=h_cool_bubble-h_cool_dew;
for i=1:n_x+n_h+n_h,
    JJ(i)=J(i)*0.01802*h_fg;
    jj(i)=i*a;
end
figure(2)
plot(jj,JJ);
set(figure(2),'Name','Heat flux');

%transllate real temperature range to 0-255 range for visualization
for ix=1:n_x,
    for iy=1:n_h+n_y,
        total_c3(iy,ix)=(total_c(iy,ix)-c_bot)/(c_top-c_bot)*255;
    end
end
figure(3)
imshow(total_c3,[0,255])
```